

The Liver Tumor Segmentation Benchmark (LiTS)

Patrick Bilic^{†*a}, Patrick Christ^{†*a}, Hongwei Bran Li^{*a,b}, Eugene Vorontsov^{†*c}, Avi Ben-Cohen^{†e},
 Georgios Kaissis^{†j,l,o}, Adi Szeskin^{†r}, Colin Jacobs^{†d}, Gabriel Efrain Humpire Mamani^{†d},
 Gabriel Chartrand^{†z}, Fabian Lohöfer^{†l}, Julian Walter Holch^{†ac,ad,bq}, Wieland Sommer^{†af},
 Felix Hofmann^{†ae,af}, Alexandre Hostettler^{†aj}, Naama Lev-Cohain^{†al}, Michal Drozdal^{†ah}, Michal Marianne
 Amitai^{†ai}, Refael Vivanti^{†ak}, Jacob Sosna^{†al}, Ivan Ezhov^a, Anjany Sekuboyina^{a,b}, Fernando Navarro^{a,bx,bz},
 Florian Kofler^{a,m,be,bz}, Johannes C. Paetzold^{o,p}, Suprosanna Shit^a, Xiaobin Hu^a, Jana Lipková^q,
 Markus Rempfler^a, Marie Piraud^{be,a}, Jan Kirschke^m, Benedikt Wiestler^m, Zhiheng Zhangⁿ,
 Christian Hülsemeyer^a, Marcel Beetz^a, Florian Ettl^{inger}^a, Michela Antonelliⁱ, Woong Bae^{bu},
 Míriam Bellver^{aq}, Lei Bi^{bi}, Hao Chen^{am}, Grzegorz Chlebus^{bj,bl}, Erik B. Dam^{bt}, Qi Dou^{ao}, Chi-Wing Fu^{ao},
 Bogdan Georgescu^{bh}, Xavier Giró-i-Nieto^{as}, Felix Gruen^{ab}, Xu Han^{by}, Pheng-Ann Heng^{ao},
 Jürgen Hesser^{av,aw,ax}, Jan Hendrik Moltz^{bj}, Christian Igel^{bt}, Fabian Isensee^{bq,br}, Paul Jäger^{bq,br},
 Fucang Jia^{bw}, Krishna Chaitanya Kaluva^u, Mahendra Khened^u, Ildoo Kim^{bu}, Jae-Hun Kim^{ba},
 Sungwoong Kim^{bu}, Simon Kohl^{bq}, Tomasz Konopczynski^{aw}, Avinash Kori^u, Ganapathy Krishnamurthi^u,
 Fan Li^v, Hongchao Li^k, Junbo Li^h, Xiaomeng Li^{an}, John Lowengrub^{bn,bo,bp}, Jun Ma^{bb},
 Klaus Maier-Hein^{bq,br,g}, Kevis-Kokitsi Maninis^{ar}, Hans Meine^{bj,bm}, Dorit Merhof^{bv}, Akshay Pai^{bt}, Mathias
 Perslev^{bt}, Jens Petersen^{bq}, Jordi Pont-Tuset^{ar}, Jin Qi^{bd}, Xiaojuan Qi^{an}, Oliver Rippel^{bv}, Karsten Roth^{au},
 Ignacio Sarasua^{ay,l}, Andrea Schenk^{bj,bk}, Zengming Shen^{bg,bh}, Jordi Torres^{at,aq}, Christian Wachinger^{ay,l,a},
 Chunliang Wang^{ap}, Leon Weninger^{bv}, Jianrong Wu^y, Daguang Xu^{bs}, Xiaoping Yang^{bc}, Simon Chun-Ho
 Yu^{bf}, Yading Yuan^{az}, Miao Yue^t, Liping Zhang^{bf}, Jorge Cardosoⁱ, Spyridon Bakas^{s,w,x},
 Rickmer Braren^{†f,l,ad}, Volker Heinemann^{†ag}, Christopher Pal^{†c}, An Tang^{†aa}, Samuel Kadoury^{†c},
 Luc Soler^{†aj}, Bram van Ginneken^{†d}, Hayit Greenspan^{†e}, Leo Joskowicz^{†r}, Bjoern Menze^{†a,b}

^aDepartment of Informatics, Technical University of Munich, Germany.

^bDepartment of Quantitative Biomedicine, University of Zurich, Switzerland.

^cEcole Polytechnique de Montréal, Canada

^dDepartment of Medical Imaging, Radboud University Medical Center, Nijmegen, the Netherlands

^eDepartment of Biomedical Engineering, Tel-Aviv University, Israel

^fGerman Cancer Consortium (DKTK)

^gPattern Analysis and Learning Group, Department of Radiation Oncology, Heidelberg University Hospital, Heidelberg, Germany

^hPhilips Research China, Philips China Innovation Campus, Shanghai, China

ⁱSchool of Biomedical Engineering & Imaging Sciences, King's College London, London, UK

^jInstitute for AI in Medicine, Technical University of Munich, Germany

^kDepartment of Computer Science, Guangdong University of Foreign Studies, China

^lInstitute for diagnostic and interventional radiology, Klinikum rechts der Isar, Technical University of Munich, Germany

^mInstitute for diagnostic and interventional neuroradiology, Klinikum rechts der Isar, Technical University of Munich, Germany

ⁿDepartment of Hepatobiliary Surgery, the Affiliated Drum Tower Hospital of Nanjing University Medical School, China.

^oDepartment of Computing, Imperial College London, London, United Kingdom

^pInstitute for Tissue Engineering and Regenerative Medicine, Helmholtz Zentrum München, Neuherberg, Germany

^qBrigham and Women's Hospital, Harvard Medical School, USA

^rSchool of Computer Science and Engineering, the Hebrew University of Jerusalem, Israel

^sCenter for Biomedical Image Computing and Analytics (CBICA), University of Pennsylvania, PA, USA

^tCGG Services (Singapore) Pte. Ltd., Singapore

^uMedical Imaging and Reconstruction Lab, Department of Engineering Design, Indian Institute of Technology Madras, India

^vSensetime, Shanghai, China

^wDepartment of Radiology, Perelman School of Medicine, University of Pennsylvania, USA

^xDepartment of Pathology and Laboratory Medicine, Perelman School of Medicine, University of Pennsylvania, PA, USA

^yTencent Healthcare (Shenzhen) Co., Ltd, China

^zThe University of Montréal Hospital Research Centre (CRCHUM) Montréal, Québec, Canada

^{aa}Department of Radiology, Radiation Oncology and Nuclear Medicine, University of Montréal, Canada

^{ab}Institute of Control Engineering, Technische Universität Braunschweig, Germany

† Organization team and data contributor.

* Patrick Bilic, Patrick Christ, Hongwei Bran Li, and Eugene Vorontsov made equal contributions to this work.

- ^{ac}Department of Medicine III, University Hospital, LMU Munich, Munich, Germany
^{ad}Comprehensive Cancer Center Munich, Munich, Germany
^{ae}Department of General, Visceral and Transplantation Surgery, University Hospital, LMU Munich, Germany
^{af}Department of Radiology, University Hospital, LMU Munich, Germany
^{ag}Department of Hematology/Oncology & Comprehensive Cancer Center Munich, LMU Klinikum Munich, Germany
^{ah}Polytechnique Montréal, Mila, QC, Canada
^{ai}Department of Diagnostic Radiology, Sheba Medical Center, Tel Aviv university, Israel
^{aj}Department of Surgical Data Science, Institut de Recherche contre les Cancers de l'Appareil Digestif (IRCAD), France
^{ak}Rafael Advanced Defense System, Israel
^{al}Department of Radiology, Hadassah University Medical Center, Jerusalem, Israel
^{am}Department of Computer Science and Engineering, The Hong Kong University of Science and Technology, China
^{an}Department of Electrical and Electronic Engineering, The University of Hong Kong, China
^{ao}Department of Computer Science and Engineering, The Chinese University of Hong Kong, Hong Kong, China
^{ap}Department of Biomedical Engineering and Health Systems, KTH Royal Institute of Technology, Sweden
^{aq}Barcelona Supercomputing Center, Barcelona, Spain
^{ar}Eidgenössische Technische Hochschule Zurich (ETHZ), Zurich, Switzerland
^{as}Signal Theory and Communications Department, Universitat Politècnica de Catalunya, Catalonia/Spain
^{at}Universitat Politècnica de Catalunya, Catalonia/Spain
^{au}University of Tuebingen, Germany
^{av}Mannheim Institute for Intelligent Systems in Medicine, department of Medicine Mannheim, Heidelberg University
^{aw}Interdisciplinary Center for Scientific Computing (IWR), Heidelberg University
^{ax}Central Institute for Computer Engineering (ZITI), Heidelberg University
^{ay}Department of Child and Adolescent Psychiatry, Ludwig-Maximilians-Universität, Munich, Germany
^{az}Department of Radiation Oncology, Icahn School of Medicine at Mount Sinai, New York, USA
^{ba}Department of Radiology, Samsung Medical Center, Sungkyunkwan University School of Medicine, Korea
^{bb}Department of Mathematics, Nanjing University of Science and Technology, China
^{bc}Department of Mathematics, Nanjing University, China
^{bd}School of Information and Communication Engineering, University of Electronic Science and Technology of China, China
^{be}Helmholtz AI, Helmholtz Zentrum München, Neuherberg, Germany
^{bf}Department of Imaging and Interventional Radiology, Chinese University of Hong Kong, Hong Kong, China
^{bg}Beckman Institute, University of Illinois at Urbana-Champaign, USA
^{bh}Siemens Healthineers, USA
^{bi}School of Computer Science, the University of Sydney
^{bj}Fraunhofer MEVIS, Bremen, Germany
^{bk}Institute for Diagnostic and Interventional Radiology, Hannover Medical School, Hannover, Germany
^{bl}Diagnostic Image Analysis Group, Radboud University Medical Center, Nijmegen, The Netherlands
^{bm}Medical Image Computing Group, FB3, University of Bremen, Germany
^{bn}Departments of Mathematics, Biomedical Engineering, University of California, Irvine, USA
^{bo}Center for Complex Biological Systems, University of California, Irvine, USA
^{bp}Chao Family Comprehensive Cancer Center, University of California, Irvine, USA
^{bq}Division of Medical Image Computing, German Cancer Research Center (DKFZ), Heidelberg, Germany
^{br}Helmholtz Imaging, Germany
^{bs}NVIDIA, Santa Clara, CA, USA
^{bt}Department of Computer Science, University of Copenhagen, Denmark
^{bu}Kakao Brain, Korea
^{bv}Institute of Imaging & Computer Vision, RWTH Aachen University, Germany
^{bw}Shenzhen Institute of Advanced Technology, Chinese Academy of Sciences
^{bz}Department of Radinology and Radiation Therapy, Klinikum rechts der Isar, Technical University of Munich, Germany
^{by}Department of computer science, UNC Chapel Hill, USA
^{bz}TranslaTUM - Central Institute for Translational Cancer Research, Technical University of Munich, Germany

Abstract

In this work, we report the set-up and results of the Liver Tumor Segmentation Benchmark (LiTS), which was organized in conjunction with the IEEE International Symposium on Biomedical Imaging (ISBI) 2017 and the International Conferences on Medical Image Computing and Computer-Assisted Intervention (MICCAI) 2017 and 2018. The image dataset is diverse and contains primary and secondary tumors with varied sizes

and appearances with various lesion-to-background levels (hyper-/hypo-dense), created in collaboration with seven hospitals and research institutions. Seventy-five submitted liver and liver tumor segmentation algorithms were trained on a set of 131 computed tomography (CT) volumes and were tested on 70 unseen test images acquired from different patients. We found that not a single algorithm performed best for both liver and liver tumors in the three events. The best liver segmentation algorithm achieved a Dice score of 0.963, whereas, for tumor segmentation, the best algorithms achieved Dices scores of 0.674 (ISBI 2017), 0.702 (MICCAI 2017), and 0.739 (MICCAI 2018). Retrospectively, we performed additional analysis on liver tumor detection and revealed that not all top-performing segmentation algorithms worked well for tumor detection. The best liver tumor detection method achieved a lesion-wise recall of 0.458 (ISBI 2017), 0.515 (MICCAI 2017), and 0.554 (MICCAI 2018), indicating the need for further research. LiTS remains an active benchmark and resource for research, e.g., contributing the liver-related segmentation tasks in <http://medicaldecathlon.com/>. In addition, both data and online evaluation are accessible via www.lits-challenge.com.

Keywords: Segmentation, Liver, Liver tumor, Deep learning, Benchmark, CT

This is a pre-print of the journal article published in *Medical Image Analysis*. If you wish to cite this work, please cite its journal version available here: <https://doi.org/10.1016/j.media.2022.102680>. This work is available under CC-BY-NC-ND license.

1. Introduction

Background. The liver is the largest solid organ in the human body and plays an essential role in metabolism and digestion. Worldwide, primary liver cancer is the second most common fatal cancer (Stewart & Wild, 2014). Computed tomography (CT) is a widely used imaging tool to assess liver morphology, texture, and focal lesions (Hann et al., 2000). Anomalies in the liver are essential biomarkers for initial disease diagnosis and assessment in both primary and secondary hepatic tumor disease (Heimann et al., 2009). The liver is a site for primary tumors that start in the liver. In addition, cancer originating from other abdominal organs, such as the colon, rectum, and pancreas, and distant organs, such as the breast and lung, often metastasize to the liver during disease. Therefore, the liver and its lesions are routinely analyzed for comprehensive tumor staging. The standard Response Evaluation Criteria in Solid Tumor (RECIST) or modified RECIST protocols require measuring the diameter of the largest target lesion (Eisenhauer et al., 2009). Hence, accurate and precise segmentation of focal lesions is required for cancer diagnosis, treatment planning, and monitoring of the treatment response. Specifically, localizing the tumor lesions in a given image scan is a prerequisite for many treatment options such as thermal percutaneous ablation (Shiina et al., 2018), radiotherapy, surgical resection (Albain et al., 2009) and arterial embolization (Viridis et al., 2019). Like many other medical imaging applications, manual delineation of the target lesion in 3D CT scans

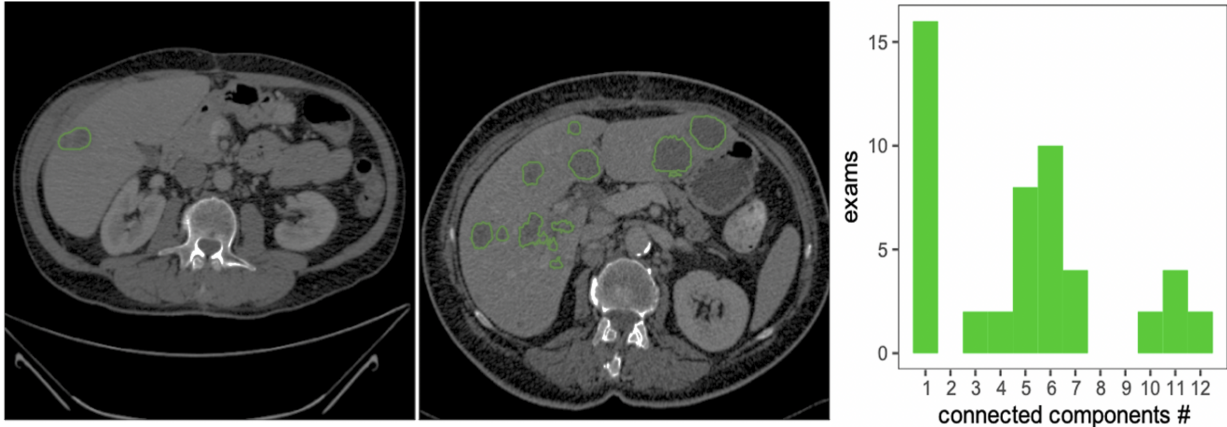


Figure 1: Example from the LiTS dataset depicting a variety of shapes of on contrast-enhanced abdominal CT scans acquired. While most exams in the dataset contain only one lesion, a large group of patients with some (2-7) or many (10-12) lesions, as shown in the histogram calculated over the whole dataset.

is time-consuming, poorly reproducible (Todorov et al., 2020) and segmentation shows operator-dependent results.

Technical challenges. Fully automated segmentation of the liver and its lesions remain challenging in many aspects. First, the variations in the lesion-to-background contrast (Moghbel et al., 2017) can be caused by: a) varied contrast agents, b) variations in contrast enhancement due to different injection timing, and c) different acquisition parameters (e.g., resolution, mAs and kVp exposure, reconstruction kernels). Second, the coexistence of different types of focal lesions (benign *vs.* malignant and tumor sub-types) with varying image appearances presents an additional challenge for automated lesion segmentation. Third, the liver tissue background signal can vary substantially in the presence of chronic liver disease, which is a common precursor of liver cancer. It is observed that many algorithms struggle with disease-specific variability, including the differences in size, shape, and the number of lesions, as well as with modifications in shape and appearance to the liver organ itself induced by treatment (Moghbel et al., 2017). Examples of differences in liver and tumor appearance in two patients are depicted in Figure 1, demonstrating the challenges of generalizing to unseen test cases with varying lesions.

Contributions. In order to evaluate the state-of-the-art methods for automated liver and liver tumor segmentation, we organized the Liver Tumor Segmentation Challenge (LiTS) in three events: 1) in conjunction with the IEEE International Symposium on Biomedical Imaging (ISBI) 2017, 2) with MICCAI 2017 and 3) as a dedicated challenge task on liver and liver tumor segmentation in the Medical Segmentation Decathlon 2018 in MICCAI 2018 (Antonelli et al., 2022).

In this paper, we describe the three key contributions to fully automated liver and liver tumor segmentation. First, we generate a new public multi-center dataset of 201 abdominal CT Volumes and the reference segmentations of liver and liver tumors. Second, we present the set-up and the summary of our LiTS benchmarks in three grand challenges. Third, we review, evaluate, rank, and analyze the resulting state-of-the-art algorithms and results. The paper is structured as follows: [Section II](#) reviews existing public datasets and state-of-the-art automated liver and liver tumors segmentation. Next, [Section III](#) describes the LiTS challenge setup, the released multi-center datasets, and the evaluation process. [Section IV](#) reports results, analyzes the liver tumor detection task, showcases critical cases in the LiTS Challenge results, and discusses the technical trends and challenges in liver tumor segmentation. [Section V](#) discusses the limitations, summarizes this work, and points to future work.

Table 1: Overview of publicly available medical datasets of liver and liver tumor images. The LiTS dataset offers a comparably large amount of 3D scans, including liver and liver tumor annotations.

Dataset	Institution	Liver	Tumor	Segmentation	#Volumes	Modality
TCGA-LIHC (Erickson et al., 2016)	TCIA	✓	✓	✗	1688	CT, MR, PT
MIDAS (Cleary, 2017)	IMAR	✓	✓	✗	4	CT
3Dircadb-01 and 3Dircadb-02 (Soler et al., 2010)	IRCAD	✓	✓	✓	22	CT
SLIVER'07 (Heimann et al., 2009)	DKFZ	✓	✗	✓	30	CT
LTSC'08 (Heimann et al., 2009)	Siemens	✗	✓	✓	30	CT
ImageCLEF'15 (imageclef.org/2015)	Bogazici Uni.	✓	✗	✓	30	CT
VISCERAL'16 (Jimenez-del Toro et al., 2016)	Uni. of Geneva	✓	✗	✓	60/60	CT/MRI
CHAOS'19 (Kavur et al., 2021)	Dokuz Eylul Uni.	✓	✗	✓	40/120	CT/MRI
LiTS	TUM	✓	✓	✓	201	CT

2. Prior Work: Datasets & Approaches

2.1. Publicly available liver and liver tumor datasets.

Compared to other organs, available liver datasets offer either a relatively small number of images and reference segmentation or provide no reference segmentation (see [Table 1](#)). The first grand segmentation challenge - SLIVER07 was held in MICCAI 2007 ([Heimann et al., 2009](#)), including the 30 CT liver images for automated segmentation. In MICCAI 2008, the LTSC'08 segmentation challenge offered 30 CT volumes with a focus on tumor segmentation ([Deng & Du, 2008](#)). The ImageCLEF 2015 liver CT reporting benchmark ¹ made 50 volumes available for computer-aided structured reporting instead of segmentation. The VISCERAL ([Jimenez-del Toro et al., 2016](#)) challenge provided 60 scans per two modalities (MRI and CT) for anatomical structure segmentation and landmark detection. The recent CHAOS challenge ([Kavur et al., 2021](#)) provide 40 CT volumes and 120 MRI volumes for *healthy* abdominal organ segmentation. However,

¹<https://www.imageclef.org/2015/liver>

none of these datasets represents well-defined cohorts of patients with lesions, and segmentation of the liver and its lesions are absent.

2.2. Approaches for liver and liver tumour segmentation

Before 2016, most automated liver and tumor segmentation methods used traditional machine learning methods. However, since 2016 and the first related publications at MICCAI (Christ et al.), deep learning methods have gradually become a methodology of choice. The following section provides an overview of published automated liver and liver tumor segmentation methods.

2.2.1. Liver segmentation

Published work on liver segmentation methods can be grouped into three categories based on: (1) prior shape and geometric knowledge, (2) intensity distribution and spatial context, and (3) deep learning.

Methods based on shape and geometric prior knowledge. Over the last two decades, statistical shape models (SSMs) (Cootes et al., 1995) have been used for automated liver segmentation tasks. However, deformation limitations prevent SSMs from capturing the high variability of the liver shapes. To overcome this issue, SSM approaches often rely on additional steps to obtain a finer segmentation contour. Therefore SSMs followed by a deformable model performing free form deformation became a valuable method for liver segmentation (Heimann et al., 2006; Kainmüller et al., 2007; Zhang et al., 2010; Tomoshige et al., 2014; Wang et al., 2015). Moreover, variations and further enhancement of SSMs such as 3D-SSM based on an intensity profiled appearance model (Lamecker et al., 2004), incorporating non-rigid template matching (Saddi et al., 2007), initialization of SSMs utilizing an evolutionary algorithm (Heimann et al., 2007), hierarchical SSMs (Ling et al., 2008), and deformable SSMs (Zhang et al., 2010) had been proposed to solve liver segmentation tasks automatically. SSMs-based methods showed the best results in SLIVER07, the first grand challenge held in MICCAI 2007 (Heimann et al., 2009; Dawant et al., 2007).

Methods based on intensity distribution and spatial context. A probabilistic atlas (PA) is an anatomical atlas with parameters that are learned from a training dataset. Park et al. proposed the first PA utilizing 32 abdominal CT series for registration based on mutual information and thin-plate splines as warping transformations (Park et al., 2003) and a Markov random field (MRF) (Park et al., 2003) for segmentation. Further proposed atlas-based methods differ in their computation of the PA and how the PA is incorporated into the segmentation task. Furthermore, PA can incorporate relations between adjacent abdominal structures to define an anatomical structure surrounding the liver (Zhou et al., 2006). Multi-atlas methods improved liver segmentation results by using non-rigid registration with a B-spline transformation model (Slagmolen et al., 2007), dynamic atlas selection and label fusion (Xu et al., 2015), or liver and non-liver voxel classification based on k-Nearest Neighbors (van Rikxoort et al., 2007).

Graph cut methods offer an efficient way to binary segmentation problems, initialized by adaptive thresholding (Massoptier & Casciari, 2007) and supervoxel (Wu et al., 2016).

Methods based on deep learning. In contrast to the methods above, deep learning, especially convolutional neural networks (CNN), is a data-driven method that can be optimized end-to-end without hand-craft feature engineering (Litjens et al., 2017). The U-shape CNN architecture (Ronneberger et al., 2015) and its variants (Milletari et al., 2016; Isensee et al., 2020; Li et al., 2018a) are widely used for biomedical image segmentation and have already proven their efficiency and robustness in a wide range of segmentation tasks. Top-performing methods share the commonality of multi-stage processes, beginning with a 3D CNN for segmentation, and post-process the resulting probability maps with Markov random field (Dou et al., 2016). Many early deep learning algorithms for liver segmentation combine neural networks with dedicated post-processing routines: Christ et al. uses 3D fully connected neural networks combined with conditional random fields, Hu et al. (2016) rely on a 3D CNN followed by a surface model. In contrast, Lu et al. (2017) use a CNN regularized by a subsequent graph-cut segmentation.

2.2.2. Liver tumor segmentation

Compared to the liver, its lesions feature a more comprehensive range of shape, size, and contrast. Liver tumors can be found in almost any location, often with ambiguous boundaries. Differences in the uptake of contrast agents may introduce additional variability. Therefore liver tumor segmentation is considered to be the more challenging task. Published methods of liver tumor segmentation can be categorized into 1) thresholding and spatial regularization, 2) local features and learning algorithms, and 3) deep learning.

Methods with thresholding and spatial regularization. Based on the assumption that gray level values of tumor areas differ from pixels/voxels belonging to regions outside the tumor, thresholding is a simple yet effective tool to automatically separate tumor from liver and background, first shown by Soler et al. (Soler et al., 2001). Since then the threshold have set by histogram analysis (Ciecholewski & Ogiela, 2007), maximum variance between classes (Nugroho et al., 2008) and iterative algorithm (Abdel-massieh et al., 2010) to improve tumor segmentation results. Spatial regulation techniques rely on (prior) information about the image or morphologies, e.g., tumor size, shape, surface, or spatial information. This knowledge is used to introduce constraints in the form of regularization or penalization. Adaptive thresholding methods can be combined with model-based morphological processing for heterogeneous lesion segmentation (Moltz et al., 2008, 2009). Active contour (Kass et al., 1988) based tumor segmentation relies on shape and surface information and utilize probabilistic models (Ben-Dan & Shenhav, 2008) or histogram analysis (Linguraru et al., 2012) to create segmentation maps automatically. Level set (Osher & Sethian, 1988) methods allow numerical computations of tumor shapes without parametrization. Level set approaches for liver tumor

segmentation are combined with supervised pixel/voxel classification in 2D (Smeets et al., 2008) and 3D (Jiménez Carretero et al., 2011).

Methods using local features and learning algorithms. Clustering methods include k-means (Massoptier & Casciaro, 2008) and fuzzy c-means clustering with segmentation refinement using deformable models (Håme, 2008). Among supervised classification methods are a fuzzy classification based level set approach (Smeets et al., 2008), support vector machines in combination with a texture based deformable surface model for segmentation refinement (Vorontsov et al., 2014), AdaBoost trained on texture features (Shimizu et al., 2008) and image intensity profiles (Li et al., 2006), logistic regression (Wen et al., 2009), and random forests recursively classifying and decomposing supervoxels (Conze et al., 2017).

Methods based on deep learning. Before LiTS, deep learning methods have been rarely used for liver tumor segmentation tasks. Christ et al. was the first to use 3D U-Net for liver and liver tumor segmentation, proposing a cascaded segmentation strategy, together with a 3D conditional random field refinement. Many of the subsequent deep learning approaches were developed and tested in conjunction with the LiTS dataset.

Benefiting from the availability of the LiTS public dataset, many new deep learning solutions on liver and liver segmentation were proposed. U-Net-based architectures are extensively used and modified to improve segmentation performance. For example, the nn-UNet (Isensee et al., 2020) first presented in LiTS at MICCAI 2018, was shown to be one of the most top-performing methods in 3D image segmentation tasks. The related works will be discussed in the results section.

3. Methods

3.1. Challenge setup

The first LiTS benchmark was organized in Melbourne, Australia, on April 18, 2017, in a workshop held at the IEEE ISBI 2017 conference. During Winter 2016/2017, participants were solicited through private emails, public email lists, social media, and the IEEE ISBI workshop announcements. Participants were requested to register at our online benchmarking system hosted on CodaLab and could download annotated training data and unannotated test data. The online benchmarking platform automatically computed performance scores. They were asked to submit a four-page summary of their algorithm after successful submissions to the CodaLab platform. Following the successful submission process at ISBI 2017, the second LiTS benchmark was held on September 14, 2017, in Quebec City, Canada, as a MICCAI workshop. The third edition of LiTS was a part of the Medical Segmentation Decathlon at MICCAI 2018 (available at <http://medicaldecathlon.com/>).

At ISBI 2017, five out of seventeen participating teams presented their methods at the workshop. At MICCAI 2017, the LiTS challenge introduced a new benchmark task - liver segmentation. Participants

registered a new CodaLab benchmark and were asked to describe their algorithm after the submission deadline, resulting in 26 teams. The training and test data for the benchmark were identical to the ISBI benchmark. The workshop at the MICCAI 2017 was organized similarly to the ISBI edition. At MICCAI 2018, LiTS was a part of a medical image segmentation decathlon organized by King’s College London in conjunction with eleven partnerships for data donation, challenge design, and administration. The LiTS benchmark dataset described in this paper constitutes the decathlon’s liver and liver lesion segmentation tasks. However, the overall challenge also required the participants to address nine other tasks, including brain tumor, heart, hippocampus, lung, pancreas, prostate, hepatic vessel, spleen, and colon segmentation. To this end, algorithms were not necessarily optimized only for liver CT segmentation.

3.2. Dataset

Training and test cases both represented abdomen CT images. The data is licensed as CC BY-NC-SA. Only the organizers from TUM have access to the labels of test images. The participants could download annotated training data from the LiTS Challenge website ².

Contributors. The image data for the LiTS challenge are collected from seven clinical sites all over the world, including a) Rechts der Isar Hospital, the Technical University of Munich in Germany, b) Radboud University Medical Center, the Netherlands, c) Polytechnique Montréal and CHUM Research Center in Canada, d) Sheba Medical Center in Israel, e) the Hebrew University of Jerusalem in Israel, f) Hadassah University Medical Center in Israel, and g) IRCAD in France. The distribution of the number of scans per institution is described in Table 2. The LiTS benchmark dataset contains 201 computed tomography images of the abdomen, of which 194 CT scans contain lesions. All data are anonymized, and the images have been reviewed visually to preclude the presence of personal identifiers. The only processing applied to the images is a transformation into a unified NIFTY format using NiBabel in Python ³. All parties agreed to make the data publicly available; ethics approval was not required.

Data diversity. The studied cohort covers diverse types of liver tumor diseases, including primary tumor disease (such as hepatocellular carcinoma and cholangiocarcinoma) and secondary liver tumors (such as metastases from colorectal, breast and lung primary cancers). The tumors had varying lesion-to-background ratios (hyper- or hypo-dense). The images represented a mixture of pre- and post-therapy abdominal CT scans and were acquired with different CT scanners and acquisition protocols, including imaging artifacts (e.g., metal artifacts) commonly found in real-world clinical data. Therefore, it was considered to be very diverse concerning resolution and image quality. The in-plane image resolution ranges from 0.56 mm to 1.0

²www.lits-challenge.com

³<https://nipy.org/nibabel/>

Table 2: Distribution of the number of scans per institution in the train and test in the LiTS dataset.

Institutions	Train	Test
Rechts der Isar Hospital, TUM, Germany	28	28
Radboud University Medical Center, the Netherlands	48	12
Polytechnique Montreal and CHUM Research Center in Canada	30	25
IRCAD, France	20	0
Sheba Medical Center	5	5
Hebrew University of Jerusalem		
Hadassah University		
Total	131	70

Table 3: The characteristics of the LiTS training and test sets. The median values and the interquartile range (IQR) are shown for each parameter. In addition, P-values were obtained by Mann-whitney u test, describing the significance between the training set and test set shown in the last column. An alpha level of 0.05 was chosen to determine significance.

	Train	Test	p-value
In-plane resolution (mm)	0.76 (0.7, 0.85)	0.74 (0.69, 0.8)	0.042
Slice thickness (mm)	1.0 (0.8, 1.5)	1.5 (0.8, 4.0)	0.004
Volume size	512×512×432 (512×512×190 , 512×512×684)	512×512×270 (512×512×125 , 512×512×622)	0.058
Number of tumors	3 (1, 9)	5 (2, 12)	0.016
Tumor volume (mm ³)	16.11 × 10 ³ (3.40 × 10 ³ , 107.77 × 10 ³)	34.78 × 10 ³ (10.41 × 10 ³ , 98.90 × 10 ³)	0.039
Liver volume (mm ³)	1586.48 × 10 ³ ± 447.14 × 10 ³ (1337.75 × 10 ³ , 1832.46 × 10 ³)	1622.64 × 10 ³ ± 546.48 × 10 ³ (1315.94 × 10 ³ , 1977.27 × 10 ³)	0.60

mm, and 0.45 mm to 6.0 mm in slice thickness. Also, the number of axial slices ranges from 42 to 1026. The number of tumors varies between 0 and 12. The size of the tumors varies between 38 mm³ and 1231 mm³. The test set shows a higher number of tumor occurrences compared to the training set. The statistical test (p-value=0.6) shows that the liver volumes in the training and test sets do not differ significantly. The average tumor HU value is 65 and 59 in the train and test sets, respectively. The LiTS data statistics are summarized in Table 3. The training and test split is with a ratio of 2:1 and the training and test sets were similar in center distribution. Generalizability to unseen centers has, hence, not been tested in LiTS.

Annotation protocol. The image datasets were annotated manually using the following strategy: A radiologist with >3 years of experience in oncologic imaging manually labelled the datasets slice-wise using the ITK-SNAP (Yushkevich et al., 2006) software and assigning one of the labels 'Tumor' or 'Healthy Liver'. Here, the "Tumor" label included any neoplastic lesion irrespective of origin (i.e. both primary liver tumors and metastatic lesions). Any part of the image not assigned one of the aforementioned labels was considered 'Background'. The segmentations were verified by three further readers blinded to the initial segmentation, with the most senior reader serving as tie-breaker in cases of labelling conflicts. Those scans with very small

and uncertain lesion-like structures were omitted in the annotation.

3.3. Evaluation

3.3.1. Ranking strategy

The main objective of *LiTS* was to benchmark segmentation algorithms. We assessed the segmentation performance of the LiTS submissions considering three aspects: a) volumetric overlap, b) surface distance, and c) volume similarity. All the values of these metrics are released to the participating teams. Considering that the volumetric overlap is our primary interest in liver and liver tumor segmentation, for simplicity, we only use the Dice score to rank the submissions at ISBI-2017 and MICCAI-2017. However, the exact choice of evaluation metric does sometimes affect the ranking results, as different metrics are sensitive to different types of segmentation errors. Hence, we provide a post-challenge ranking, considering three properties by summing up three ranking scores and re-ranking by the final scores. The evaluation codes for all metrics can be accessed in Github ⁴.

3.3.2. Statistical tests

To compare the submissions from two teams in a *per case* manner, we used Wilcoxon signed-rank test (Rey & Neuhäuser, 2011). To compare the distributions of submissions from two years, we used the Mann-Whitney U Test (McKnight & Najab, 2010) (unpaired) for the two groups.

3.3.3. Segmentation metrics

Dice score. The Dice score evaluates the degree of overlap between the predicted and reference segmentation masks. For example, given two binary masks A and B , it is formulated as:

$$Dice(A, B) = \frac{2|A \cap B|}{|A| + |B|} \quad (1)$$

The Dice score is applied *per case* and then averaged over all cases consistently for three benchmarks. This way, the Dice score applies a higher penalty to prediction errors in cases with fewer actual lesions.

Average symmetric surface distance. Surface distance metrics are correlated measures of the distance between the surfaces of a reference and the predicted region. Let $S(A)$ denote the set of surface voxels of A . Then, the shortest distance of an arbitrary voxel v to $S(A)$ is defined as:

$$d(v, S(A)) = \min_{s_A \in S(A)} \|v - s_A\|, \quad (2)$$

where $\|\cdot\|$ denotes the Euclidean distance. The average symmetric surface distance (ASD) is then given by:

$$ASD(A, B) = \frac{1}{|S(A)| + |S(B)|} \left(\sum_{s_A \in S(A)} d(s_A, S(B)) + \sum_{s_B \in S(B)} d(s_B, S(A)) \right). \quad (3)$$

⁴<https://github.com/PatrickChrist/lits-challenge-scoring>

Maximum symmetric surface distance. The maximum symmetric surface distance (MSSD), also known as the Symmetric Hausdorff Distance, is similar to ASD except that the maximum distance is taken instead of the average:

$$MSSD(A, B) = \max \left\{ \max_{s_A \in S(A)} d(s_A, S(B)), \max_{s_B \in S(B)} d(s_B, S(A)) \right\}. \quad (4)$$

Relative volume difference. The relative volume difference (RVD) directly measures the volume difference without considering the overlap between reference A and the prediction B .

$$RVD(A, B) = \frac{|B| - |A|}{|A|}. \quad (5)$$

For the other evaluation metrics, such as tumor burden estimation and the corresponding rankings, please check the Appendix.

3.3.4. Detection metrics

Considering the clinical relevance of lesion detection, we introduce three detection metrics in the additional analysis. The metrics are calculated globally to avoid potential issues when the patient has no tumors. There must be a known correspondence between predicted and reference lesions to evaluate the lesion-wise metrics. Since *lesions* are all defined as a single binary map, this correspondence must be determined between the prediction and reference masks' connected components. Components may not necessarily have a one-to-one correspondence between the two masks. The details of the correspondence algorithm are presented in [Appendix C](#).

Individual lesions are defined as 3D connected components within an image. A lesion is considered detected if the predicted lesion has sufficient overlap with its corresponding reference lesion, measured as the intersection over the union of their respective segmentation masks. It allows for a count of true positive, false positive, and false-negative detection, from which we compute the *precision* and *recall* of lesion detection. The metrics are defined as follows:

Individual lesions are defined as 3D connected components within an image. A lesion is considered detected if the predicted lesion has sufficient overlap with its corresponding reference lesion, measured as the intersection over the union of their respective segmentation masks. It allows for a count of true positive, false positive, and false-negative detection, from which we compute the *precision* and *recall* of lesion detection. The metrics are defined as follows:

$$IoU = \frac{|A \cap B|}{|A \cup B|}. \quad (6)$$

Precision. It relates the number of true positives (TP) to false positives (FP), also known as positive predictive value:

$$precision = \frac{TP}{TP + FP}. \quad (7)$$

Recall. It relates the number of true positives (TP) to false negatives (FN), also known as sensitivity or true positive rate:

$$recall = \frac{TP}{TP + FN}. \quad (8)$$

F1 score. It measures the harmonic mean of precision and recall:

$$F1 = \frac{2}{precision^{-1} + recall^{-1}}. \quad (9)$$

3.3.5. Participating policy and online evaluation platform

The participants were allowed to submit three times per day in the test stage during the challenge week. Members of the organizers' groups could participate but were not eligible for awards. The awards were given to the top three teams for each task. The top three performing methods gave 10-min presentations and were announced publicly. For a fair comparison, the participating teams were only allowed to use the released training data to optimize their methods. All participants were invited to be co-authors of the manuscript summarizing the challenge.

A central element of LiTS was - and remains to be - its online evaluation tool hosted by CodaLab. On Codalab, participants could download annotated training and "blinded" test data and upload their segmentation for the test cases. The system automatically evaluated the uploaded segmentation maps' performance and made the overall performance available to the participants. Average scores for the different liver and lesion segmentation tasks and tumor burden estimation were also reported online on a leaderboard. Reference segmentation files for the LiTS test data were hosted on the Codalab but not accessible to participants. Therefore, the users uploaded their segmentation results through a web interface, reviewed the uploaded segmentation, and then started an automated evaluation process. The evaluation to assess the segmentation quality took approximately two minutes per volume. In addition, the overall segmentation results of the evaluation were automatically published on the Codalab leaderboard web page and could be downloaded as a csv file for further statistical analysis.

The Codalab platform remained open for further use after the three challenges and will remain so in the future. As of April 2022, it has evaluated more than 3,414 valid submissions (238,980 volumetric segmentation) and recorded over 900 registered LiTS users. The up-to-date ranking is available at Codalab for researchers to continuously monitor new developments and streamline improvements. In addition, the code to generate the evaluation metrics between reference and predictions is available as open-source at GitHub ⁵.

⁵<https://github.com/PatrickChrist/LiTS-CHALLENGE>

4. Results

4.1. Submitted algorithms and method description

The submitted methods in ISBI-2017, MICCAI-2017 and MICCAI-2018 are summarized in Table 4 and Table 5, and the reference paper of Medical Segmentation Decathlon (Antonelli et al., 2022). In the following, we grouped the algorithms with several properties.

Algorithms and architectures. Seventy-three submissions were fully automated approaches, while only one was semi-supervised (■ J. Ma *et al.*). U-Net derived architectures were overwhelmingly used in the challenge with only two automated methods using a modified VGG-net (■ J. Qi *et al.*) and a k-CNN (■ J. Lipkova *et al.*) respectively. Most submissions adopted the coarse-to-fine approach in which multiple U-nets were cascaded to perform liver and liver segmentation at different stages. Additional residual connections and adjusted input resolution were the most common changes to the basic U-Net architecture. Three submissions combined individual models as an ensemble technique. In 2017, 3D methods were not directly employed on the original image resolution by any of the submitted methods due to high computational complexity. However, some submissions used 3D convolutional neural networks solely for tumor segmentation tasks with small input patches. Instead of full 3D, other methods tried to capture the advantages of three-dimensionality by using a 2.5 D model architecture, i.e., providing a stack of images as a multi-channel input to the network and receiving the segmentation mask of the center slice of this stack as a network output.

Critical components of the segmentation methods. Data pre-processing with HU-value clipping, normalization, and standardization were the most frequent techniques in most of the methods. Data augmentation was also widely used and mainly focused on standard geometric transformations such as flipping, shifting, scaling, or rotation. Individual submissions implemented more advanced techniques such as histogram equalization and random contrast normalization. The most common optimizer varied between ADAM and Stochastic gradient descent with momentum, with one approach relying on RMSProp. Multiple loss functions were used for training, including standard and class-weighted cross-entropy, Dice loss, Jaccard loss, Tversky loss, L2 loss, and ensemble loss techniques combining multiple individual loss functions into one.

Post-processing. Some types of post-processing methods were also used by the vast majority of the algorithm. The common post-processing steps were to form connected tumor components and overlay the liver mask on the tumor segmentation to discard tumors outside the liver region. More advanced methods included a random forest classifier, morphological filtering, a particular shallow neural network to eliminate false positives or custom algorithms for tumor hole filling.

Features of top-performing methods. The best-performing methods at ISBI 2017 used cascaded U-Net approaches with short and long skip connections and 2.5D input images (■ X. Han *et al.*). In addition, weighted cross-entropy loss functions and a few ensemble learning techniques were employed by most of the top-performing methods, together with some common pre- and post-processing steps such as HU-value clipping and connected component labeling, respectively. Some top-performing submissions at MICCAI 2017 (e.g., ■ J. Zou) integrated the insights from the ISBI 2017, including the idea of the ensemble, adding residual connections, and featuring more sophisticated rule-based post-processing or classical machine learning algorithms. Therefore, the main architectural differences compared to the ISBI submissions were the higher usage of ensemble learning methods, a higher incidence of residual connections, and an increased number of more sophisticated post-processing steps. Another top-performing method by ■ X. Li *et al.* proposed a hybrid insight by integrating the advantages of the 2D and 3D networks in the 3D liver tumor segmentation task (Li *et al.*, 2018b). Therefore, compared to the methods in ISBI submissions that solely rely on 2D or 3D convolutions, the main architecture difference was the hybrid usage of 2D and 3D networks. In MICCAI-LiTS 2018, 3D deep learning models became popular and generally outperformed 2.5D or 2D without more sophisticated pre-processing steps.

Table 4: Details of the participating teams' methods in LiTS-ISBI-2017.

Lead Author & Team Members	Method, Architecture & Modifications	Data Augmentation	Loss Function	Optimizer Training	Pre-processing	Post-processing	Ensemble strategy
■ X. Han ;	Residual U-Net with 2.5D input (a stack of 5 slices)	cropping, flipping	weighted cross-entropy	SGD with momentum	Value-clipping to [-200, 200]	Connected components with maximum probability below 0.8 were removed	None
■ E. Vorontsov ; A. Tang, C. Pal, S. Kadoury	Liver FCN provides pre-trained weights for tumour FCN. Trained on 256×256 , finetuned on 512×512 .	Random flips, rotations, zooming, elastic deformations.	Dice loss	RMSprop	None	largest connected component for liver	Ensemble of three models
■ G. Chlebus ; H. Meine, J. H. Moltz, A. Schenk	Liver: 3 orthogonal 2D U-nets working on four resolution levels. Tumor: 2D U-net working on four resolution levels	Manual removal of cases with flawed reference segmentation	soft Dice	Adam	Liver: resampling to isotropic 2 mm voxels.	Tumor candidate filtering based on RF-classifier to remove false positives	For liver: majority vote
■ L. Bi ; Jinman Kim	Cascaded ResNet based on a pre-trained FCN on 2D axial slices.	Random scaling, crops and flips	cross-entropy	SGD	Value-clipping to [-160, 240]	Morphological filter to fill the holes	Multi-scale ensembling by averaging the outputs from different inputs sizes.
■ C. Wang	Cascaded 2D U-Net in three orthogonal views	Random rotation, random translation, and scaling	Soft Dice	SGD	None	None	None
■ P. Christ	Cascaded U-Net	mirror, cropping, additional noise	weighted cross-entropy	SGD with momentum		3D Conditional Random Field	
■ J. Lipkova ; M. Rempfler, J. Lowengrub, B. Menze	U-Net for liver segmentation and Cahn-Hilliard Phase field separation for lesions	None	Liver: cross-entropy; Tumor: Energy function	SGD	None	None	None
■ J. Ma ; Y. Li, Y. Wu, M. Zhang, X. Yang	Random Forest and Fuzzy Clustering	None	None	None	Value-clipping to [-160, 240] and intensity normalization to [0, 255]		
■ T. Konopczynski ; K. Roth, J. Hesser	Dense 2D U-Nets (Tiramisu)	None	Soft Tversky-Coefficient based Loss function	Adam	Value-clipping to [-100, 400]	None	None
■ M. Bellver ; K. Maninis, J. Tuset, X. Giro-i-Nieto, J. Torres	Cascaded FCN with side outputs at different resolutions. Three-channel 2D input.	None	Weighted binary cross entropy	SGD with Momentum	Value-clipping to [-150, 250] and intensity normalization to [0, 255]	Component analysis to remove false positives. 3D CRF.	None
■ J. Qi ; M. Yue	A pretrained VGG with concatenated multi-scale feature maps	None	binary cross entropy	SGD	None	None	None

Table 5: Details of the participating teams' methods in LiTS-MICCAI-2017.

Lead Author & Team Members	Method, Architecture & Modifications	Data Augmentation	Loss Function	Optimizer Training	Pre-processing	Post-processing	Ensemble strategy
■ Y. Yuan;	Hierarchical 2.5D FCN network	flipping, shifting, rotating, scaling and random contrast normalization	Jaccard distance	Adam	Clipping HU values to [-100, 400]	None	ensembling 5 models from 5-fold cross validation
■ A. Ben-Cohen;	VGG-16 as a backbone and 3-channel input	scaling	softmax log loss	SGD	Clipping HU values to [-160, 240]	None	None
■ J. Zou;	Cascaded U-Nets	weighted cross-entropy	Adam		Clipping HU values to [-75, 175]	hole filling and noise removal	ensemble of two model with different inputs
■ X. Li, H. Chen, X. Qi, Q. Dou, C. Fu, P. Heng	H-DenseUNet (Li et al., 2018b)	rotation, flipping, scaling	Cross-entropy	SGD	Clipping HU values to [-200, 250]	Largest connected component; hole filling	None
■ G. Chlebus; H. Meine, J. H. Moltz, A. Schenk	Liver: 3 orthogonal 2D U-nets working on four resolution levels. Tumor: 2D U-net working on four resolution levels (Chlebus et al., 2018)	Mannul removal of cases with flawed reference segmentation	soft Dice	Adam	Liver: resampling to isotropic 2 mm voxels.	Tumor candidate filtering based on RF-classifier to remove false positives	For liver: majority vote
■ J. Wu	Cascade 2D FCN	scaling	Dice Loss	Adam	None	None	None
■ C. Wang	Cascade 2D U-Net in three orthogonal views	Random rotation, random translation, and scaling	Soft Dice	SGD	None	None	None
■ E. Vorontsov; A. Tang, C. Pal, S. Kadoury	Liver FCN provides pre-trained weights for tumour FCN. Trained on 256×256, finetuned on 512×512.	Random flips, rotations, zooming, elastic deformations.	Dice loss	RMSprop	None	largest connected component for liver	Ensemble of three models
■ K. Roth; T. Konopczynski, J. Hesser	2D and 3D U-Net, however with an iterative Mask Mining process. similar to model boosting	flipping, rotation, and zooming	Mixture of smooth Dice loss and weighted cross-entropy	Adam	Clipping HU values to [-100, 600]	None	None
■ X. Han;	Residual U-Net with 2.5D input (a stack of 5 slices)	cropping, flipping	weighted cross-entropy	SGD with momentum	Value-clipping to [-200, 200]	Connected components with maximum probability below 0.8 were removed	None
■ J. Lipkova; M. Rempfler, J. Lowengrub	U-Net for liver segmentation and Cahn-Hilliard Phase field separation for lesions	None	Liver:cross-entropy; Tumor: Energy function	SGD	None	None	None
■ L. Bi; Jinman Kim	Cascaded ResNet based on a pre-trained FCN on 2D axial slices.	Random scaling, crops and flips	cross-entropy	SGD	Value-clipping to [-160, 240]	Morphological filter to fill the holes	Multi-scale ensembling by averaging the outputs from different inputs sizes.
■ M. Piraud; A. Sekuboyina, B. Menze	U-Net with a double sigmoid activation	None	weighted cross-entropy	Adam	Value-clipping to [-100, 400]; intensity normalization	None	None
■ J. Ma; Y. Li, Y. Wu, M. Zhang, X. Yang	Label propagation (Interactive method)	None	None	None	Value-clipping to [-100, 400]; intensity normalization	None	None
■ L. Zhang; S. C. YU	Context-aware PolyUNet with zooming out/in and two-stage strategy (Zhang & Yu, 2021)	Weighted cross-entropy	SGD	Value-clipping to [-200, 300]	largest connected component	None	

4.2. Results of individual challenges

At ISBI 2017 and MICCAI 2017, the LiTS challenges received 61 valid submissions and 32 contributing short papers as part of the two workshops. At MICCAI 2018, LiTS was held as part of the Medical Segmentation Decathlon and received 18 submissions (one of them was excluded from the analysis as requested by the participating team). In this work, the segmentation results were evaluated based on the same metrics described to ensure the comparability between the three events. For ISBI 2017, no liver segmentation task was evaluated. The results of the tumor segmentation task were shown for all the events, i.e., ISBI 2017, MICCAI 2017, and MICCAI 2018.

4.2.1. Liver segmentation

Overview. The results of the liver segmentation task showed high Dice scores; most teams achieved more than 0.930. It indicated that solely using the Dice score could not distinguish a clear winner. When we compared the progress with the two LiTS benchmarks, the results of MICCAI 2017 were slightly better than the MICCAI-MSD 2018 in terms of ASD (1.104 *vs.* 1.342). It might be because the algorithms for MICCAI-MSD were optimized considering their generalizability on different organs and imaging modalities. In contrast, the methods for MICCAI 2017 were specifically optimized for liver and CT imaging. The ranking result is shown in Table 6.

LiTS-MICCAI 2017. The evaluation of the liver segmentation task relied on the three metrics explained in the previous chapter, with the Dice score per case acting as the primary metric used for the final ranking. Almost all methods except the last three achieved Dice per case values above 0.920, with the best one scoring 0.963. Ranking positions remain relatively stable when ordering submissions according to the other surface distance metric. Most methods changed by a few spots, and the top four methods were only interchanging positions among themselves. The position variation was more significant than the Dice score when using the surface distance metric ASD for the ranking, with some methods moving up to 4 positions. However, on average, the top-2 performing Dice per case methods still achieved the lowest surface distance values, with the winning method retaining the top spot in two rankings.

LiTS-MICCAI-MSD 2018. The performance of Decathlon methods in liver segmentation showed similar results compared to MICCAI 2017. In both challenges, one could observe that the difference in Dice scores between top-performing methods was insignificant mainly because the liver is a large organ. The comparison of ASD between MICCAI 2018 and MICCAI 2017 confirmed that state-of-the-art methods could automatically segment the liver with similar performance to manual expert annotation for most cases. However, the methods exclusively trained for liver segmentation in MICCAI 2017 showed better segmentations under challenging cases (1.104 *vs.* 1.342).

4.2.2. Liver tumor segmentation and detection

Overview. While automated liver segmentation methods showed promising results (comparable to expert annotation), the liver tumor segmentation task remained room for improvement. To illustrate the difficulty of detecting small lesions, we grouped the lesions into three categories with a clinical standard: a) small lesions less than 10 mm in diameter, b) medium lesions between 10 mm and 20 mm in diameter, and c) large lesion bigger than 20 mm in diameter. The ranking result is shown in Table 7.

LiTS-ISBI 2017. The highest Dice scores for liver tumor segmentation were in the middle 0.60s range, with the winner team achieving a score of 0.674 followed by 0.652 and 0.645 for the second and third places, respectively. However, there were no statistically significant differences between the top three teams in all three metrics. The final ranking changed to some degree when considering the ASD metric. For example, Bi *et al.* obtained the best ASD score but retained its order with the best methods overall. In lesion detection, we found that detecting small lesions was very challenging in which top-performing teams achieved only around 0.10 in F1 score. Figure 6 shows some sample results of the top-performing methods.

LiTS-MICCAI 2017. The best tumor segmentation Dice scores improved significantly compared to ISBI, with MICCAI’s highest average Dice (per case) of 0.702 compared to 0.674 in ISBI on the same test set. However, the ASD metric did not improve (1.189 *vs.* 1.118) on the best top-performing method. In addition, there were no statistically significant differences between the top three teams in all three metrics. There was an overall positive correlation of ranking positions with submissions that performed well at the liver segmentation task concerning the liver tumor segmentation task. A weak positive correlation between the Dice ranking and the surface distance metrics could still be observed, although a considerable portion of methods changes positions by more than a few spots. The detection performance in MICCAI 2017 showed improvement over ISBI 2017 in lesion recall (0.479 *vs.* 0.458 for the best team). Notably, the best-performing team (■ J. Zou *et al.*) achieved a very low precision of 0.148, which indicated that the method generates many false positives. Figure 7 shows some sample results of the top-performing methods.

LiTS-MICCAI-MSD 2018. The LiTS evaluation of MICCAI 2018 was integrated into MSD and attracted much attention, receiving 18 valid submissions. Methods were ranked according to two metrics: Dice score and ASD (in liver and liver tumor segmentation tasks). Compared to MICCAI 2017 and ISBI 2016, the two top-performing teams significantly improved the Dice scores (0.739 and 0.721 *vs.* 0.702) and ASD (0.903 and 0.896 *vs.* 1.189). However, there were no statistically significant differences between the top two teams in all three metrics. The first place (F. Isensee *et al.*) statistically significant (p -value < 0.001) outperformed the third place (S. Chen *et al.*) considering Dice score. More importantly, the same team won the two tasks using a self-adapted 3D deep learning solution, indicating a step forward in the development of segmentation

methodology. The detection performance in MICCAI 2018 showed improvement over MICCAI 2017 in lesion recall (0.554 *vs.* 0.479 for the best-performing teams).

From the scatter plots shown in Figure 2, we observed that not all the top-performing methods in three LiTS challenges achieved good scores on tumor detection. The behavior of distance- and overlap-based metrics was similar. The detection metrics with clinical relevance could prevent the segmentation model from tending to segment large lesions. Thus it should be considered when ranking participating teams and performing the comprehensive assessment.

Table 6: Liver segmentation submissions of LiTS–MICCAI 2017 and LiTS–MICCAI–MSD 2018 ranked by Dice score and ASD. Top-performing teams in liver segmentation tasks are highlighted with blue in each metric. A ranking score follows each metric value in the bracket. *Re-ranking** denotes a post-challenge ranking considering two metrics by averaging the ranking scores. Notably only Dice and RVD are considered as the volume difference of the liver is not of interest, as opposed to the liver tumor.

	Ranking	Ref. Name	Dice	ASD	Re-ranking*
LiTS-MICCAI 2017	1	Y. Yuan <i>et al.</i>	0.963 (1)	1.104 (1)	2 (1)
	2	A. Ben-Cohen <i>et al.</i>	0.962 (2)	1.130 (2)	4 (2)
	3	J. Zou <i>et al.</i>	0.961 (3)	1.268 (4)	7 (3)
	4	X. Li <i>et al.</i>	0.961 (3)	1.692 (8)	10 (4)
	5	L. Zhang <i>et al.</i>	0.960 (4)	1.510 (7)	11 (5)
	6	G. Chlebus <i>et al.</i>	0.960 (4)	1.150 (3)	7 (3)
	7	J. Wu <i>et al.</i>	0.959 (5)	1.311 (5)	10 (4)
	8	C. Wang <i>et al.</i>	0.958 (6)	1.367 (6)	12 (6)
	9	E. Vorontsov <i>et al.</i>	0.951 (7)	1.785 (9)	16 (7)
	10	K. Kaluva <i>et al.</i>	0.950 (8)	1.880 (10)	18 (8)
	11	K. Roth <i>et al.</i>	0.946 (9)	1.890 (11)	20 (9)
	12	X. Han <i>et al.</i>	0.943 (10)	2.890 (12)	22 (10)
	13	J. Lipkova <i>et al.</i>	0.938 (11)	3.540 (13)	24 (11)
	14	L. Bi <i>et al.</i>	0.934 (12)	258.598 (15)	26 (12)
	15	M. Piraud <i>et al.</i>	0.767 (13)	37.450 (14)	26 (12)
	16	J. Ma <i>et al.</i>	0.041 (14)	8231.318 (15)	29 (13)
LiTS-MICCAI 2018	1	F. Isensee <i>et al.</i>	0.962 (1)	2.565 (9)	10 (5)
	2	Z. Xu <i>et al.</i>	0.959 (2)	1.342 (1)	3 (1)
	3	D. Xu <i>et al.</i>	0.959 (2)	1.722 (5)	7 (3)
	4	B. Park <i>et al.</i>	0.955 (3)	1.651 (4)	7 (3)
	5	S. Chen <i>et al.</i>	0.954 (4)	1.386 (2)	6 (2)
	6	R. Chen <i>et al.</i>	0.954 (5)	1.435 (3)	8 (4)
	7	M. Perslev <i>et al.</i>	0.953 (6)	2.360 (8)	14 (6)
	8	I. Kim <i>et al.</i>	0.948 (7)	2.942 (12)	19 (8)
	9	O. Kodym <i>et al.</i>	0.942 (8)	2.710 (11)	19 (8)
	10	F. Jia <i>et al.</i>	0.942 (9)	2.198 (6)	15 (7)
	11	S. Kim <i>et al.</i>	0.934 (10)	6.937 (14)	24 (10)
	12	W. Bae <i>et al.</i>	0.934 (11)	2.615 (10)	21 (9)
	13	Y. Wang <i>et al.</i>	0.926 (12)	2.313 (7)	19 (8)
	14	I. Sarasua <i>et al.</i>	0.924 (13)	6.273 (13)	26 (11)
	15	O. Rippel <i>et al.</i>	0.904 (14)	16.163 (16)	30 (12)
	16	R. Rezaeifar <i>et al.</i>	0.864 (15)	9.358 (15)	30 (12)
	17	J. Ma <i>et al.</i>	0.706 (16)	159.314 (17)	33 (13)

4.3. Meta Analysis

In this section, we focus on liver tumor segmentation and analyze the inter-rater variability and method development during the last six years.

Table 7: Liver tumor segmentation results of three challenges ranked by segmentation metrics (i.e., Dice, ASD and RVD) and detection metrics (i.e., precision, recall and separated F1 scores with three different sizes of lesion). Each metric value is followed by a ranking score in the bracket. Top performing teams in tumor segmentation and tumor detection are highlighted with blue and pink colors in each metric, respectively. *Re-ranking** denotes a post-challenge ranking considering three metrics by averaging the ranking scores.

Ranking	Ref. Name	Dice	ASD	RVD	Re-ranking*	Precision	Recall	F1 _{small}	F1 _{medium}	F1 _{large}	
LITS-ISBI 2017	1	X. Han <i>et al.</i>	0.674 (1)	1.118 (3)	-0.103 (7)	11 (3)	0.354 (4)	0.458 (1)	0.103 (3)	0.450 (1)	0.879 (1)
	2	G. Chlebus <i>et al.</i>	0.652 (2)	1.076 (2)	-0.025 (2)	6 (2)	0.385 (3)	0.406 (4)	0.116 (1)	0.421 (3)	0.867 (3)
	3	E. Vorontsov <i>et al.</i>	0.645 (3)	1.225 (6)	-0.124 (8)	17 (6)	0.529 (2)	0.439 (2)	0.109 (2)	0.369 (4)	0.850 (4)
	4	L. Bi <i>et al.</i>	0.645 (3)	1.006 (1)	0.016 (1)	5 (1)	0.316 (5)	0.431 (3)	0.057 (5)	0.441 (2)	0.876 (2)
	5	C. Wang <i>et al.</i>	0.576 (4)	1.187 (5)	-0.073 (5)	14 (5)	0.273 (6)	0.346 (7)	0.038 (7)	0.323 (5)	0.806 (7)
	6	P. Christ <i>et al.</i>	0.529 (5)	1.130 (4)	0.031 (3)	12 (4)	0.552 (1)	0.383 (5)	0.075 (4)	0.221 (7)	0.837 (6)
	7	J. Lipkova <i>et al.</i>	0.476 (6)	2.366 (8)	-0.088 (6)	20 (7)	0.105 (8)	0.357 (6)	0.054 (6)	0.250 (6)	0.843 (5)
	8	J. Ma <i>et al.</i>	0.465 (7)	2.778 (10)	0.045 (4)	21 (8)	0.107 (7)	0.080 (10)	0.000 (10)	0.033 (10)	0.361 (10)
	9	T. Konopczynski <i>et al.</i>	0.417 (8)	1.342 (7)	-0.150 (9)	24 (9)	0.057 (9)	0.189 (8)	0.014 (9)	0.106 (8)	0.628 (8)
	10	M. Bellver <i>et al.</i>	0.411 (9)	2.776 (9)	-0.263 (11)	29 (10)	0.028 (10)	0.172 (9)	0.031 (8)	0.175 (9)	0.512 (9)
	11	J. Qi <i>et al.</i>	0.188 (10)	6.118 (11)	-0.229 (10)	31 (11)	0.008 (11)	0.009 (11)	0.000 (10)	0.000 (11)	0.041 (11)
LITS-MICCAI 2017	1	J. Zou <i>et al.</i>	0.702 (1)	1.189 (8)	5.921 (10)	14 (2)	0.148 (13)	0.479 (2)	0.163 (2)	0.446 (4)	0.876 (5)
	2	X. Li <i>et al.</i>	0.686 (2)	1.073 (4)	5.164 (9)	16 (4)	0.426 (3)	0.515 (1)	0.150 (4)	0.544 (1)	0.907 (3)
	3	G. Chlebus <i>et al.</i>	0.676 (3)	1.143 (6)	0.464 (7)	16 (4)	0.519 (1)	0.463 (3)	0.129 (6)	0.494 (2)	0.836 (10)
	4	E. Vorontsov <i>et al.</i>	0.661 (4)	1.075 (5)	12.124 (15)	24 (6)	0.454 (2)	0.455 (6)	0.142 (5)	0.439 (6)	0.877 (4)
	5	Y. Yuan <i>et al.</i>	0.657 (5)	1.151 (7)	0.288 (6)	18 (5)	0.321 (5)	0.460 (5)	0.112 (8)	0.471 (3)	0.870 (8)
	6	J. Ma <i>et al.</i>	0.655 (6)	5.949 (12)	5.949 (11)	29 (9)	0.409 (4)	0.293 (14)	0.024 (13)	0.200 (13)	0.770 (13)
	7	K. Kaluva <i>et al.</i>	0.640 (7)	1.040 (2)	0.190 (4)	13 (1)	0.165 (10)	0.463 (4)	0.112 (7)	0.421 (8)	0.910 (1)
	8	X. Han <i>et al.</i>	0.630 (8)	1.050 (3)	0.170 (3)	14 (2)	0.160 (11)	0.330 (11)	0.129 (6)	0.411 (9)	0.908 (2)
	9	C. Wang <i>et al.</i>	0.625 (9)	1.260 (10)	8.300 (13)	32 (10)	0.156 (12)	0.408 (8)	0.081 (10)	0.423 (7)	0.832 (11)
	10	J. Wu <i>et al.</i>	0.624 (10)	1.232 (9)	4.679 (8)	27 (7)	0.179 (9)	0.372 (9)	0.093 (9)	0.373 (11)	0.875 (6)
	11	A. Ben-Cohen <i>et al.</i>	0.620 (11)	1.290 (11)	0.200 (5)	27 (7)	0.270 (7)	0.290 (15)	0.079 (11)	0.383 (10)	0.864 (9)
	12	L. Zhang <i>et al.</i>	0.620 (12)	1.388 (13)	6.420 (12)	37 (11)	0.239 (8)	0.446 (7)	0.152 (3)	0.445 (5)	0.872 (7)
	13	K. Roth <i>et al.</i>	0.570 (13)	0.950 (1)	0.020 (1)	15 (3)	0.070 (14)	0.300 (13)	0.167 (1)	0.411 (9)	0.786 (12)
	14	J. Lipkova <i>et al.</i>	0.480 (14)	1.330 (12)	0.060 (2)	28 (8)	0.060 (16)	0.190 (16)	0.014 (14)	0.206 (12)	0.755 (13)
	15	M. Piraud <i>et al.</i>	0.445 (15)	1.464 (14)	10.121 (14)	43 (12)	0.068 (15)	0.325 (12)	0.038 (12)	0.196 (14)	0.738 (15)
LITS-MICCAI 2018	1	F. Isensee <i>et al.</i>	0.739 (1)	0.903 (2)	-0.074 (10)	13 (2)	0.502 (4)	0.554 (1)	0.239 (1)	0.564 (1)	0.915 (2)
	2	D. Xu <i>et al.</i>	0.721 (2)	0.896 (1)	-0.002 (1)	4 (1)	0.549 (2)	0.503 (2)	0.149 (3)	0.475 (2)	0.937 (1)
	3	S. Chen <i>et al.</i>	0.611 (3)	1.397 (11)	-0.113 (12)	26 (6)	0.182 (9)	0.368 (4)	0.035 (9)	0.239 (12)	0.859 (3)
	4	B. Park <i>et al.</i>	0.608 (4)	1.157 (6)	-0.067 (8)	18 (5)	0.343 (5)	0.350 (7)	0.044 (8)	0.267 (7)	0.845 (4)
	5	O. Kodym <i>et al.</i>	0.605 (5)	1.134 (4)	-0.048 (6)	16 (3)	0.523 (3)	0.336 (8)	0.063 (7)	0.243 (10)	0.819 (6)
	6	Z. Xu <i>et al.</i>	0.604 (6)	1.240 (8)	-0.025 (4)	18 (5)	0.396 (6)	0.334 (9)	0.015 (10)	0.243 (11)	0.837 (5)
	7	R. Chen <i>et al.</i>	0.569 (7)	1.238 (7)	-0.188 (14)	28 (8)	0.339 (7)	0.427 (3)	0.207 (2)	0.366 (3)	0.804 (8)
	8	I. Kim <i>et al.</i>	0.562 (8)	1.029 (3)	0.012 (2)	13 (2)	0.594 (1)	0.360 (5)	0.092 (4)	0.328 (5)	0.781 (9)
	9	M. Perslev <i>et al.</i>	0.556 (9)	1.134 (5)	0.020 (3)	17 (4)	0.024 (17)	0.330 (10)	0.034 (10)	0.251 (8)	0.811 (7)
	10	W. Bae <i>et al.</i>	0.517 (10)	1.650 (12)	-0.039 (5)	27 (7)	0.061 (14)	0.308 (11)	0.078 (6)	0.244 (9)	0.742 (11)
	11	I. Sarasua <i>et al.</i>	0.486 (11)	1.374 (10)	-0.084 (11)	32 (10)	0.043 (16)	0.298 (12)	0.045 (8)	0.294 (6)	0.678 (12)
	12	R. Rezaeifar <i>et al.</i>	0.472 (12)	1.776 (13)	-0.258 (15)	40 (12)	0.112 (11)	0.216 (13)	0.005 (12)	0.081 (14)	0.650 (13)
	13	O. Rippel <i>et al.</i>	0.451 (13)	1.345 (9)	-0.068 (9)	31 (9)	0.044 (15)	0.356 (6)	0.083 (5)	0.353 (4)	0.771 (10)
	14	S. Kim <i>et al.</i>	0.404 (14)	1.891 (14)	0.151 (13)	41 (13)	0.116 (10)	0.170 (14)	0.005 (12)	0.091 (13)	0.589 (14)
	15	F. Jia <i>et al.</i>	0.316 (15)	12.762 (16)	-0.620 (16)	47 (14)	0.069 (12)	0.011 (17)	0.015 (10)	0.000 (16)	0.024 (17)
	16	Y. Wang <i>et al.</i>	0.311 (16)	2.105 (15)	0.054 (7)	38 (11)	0.154 (8)	0.068 (15)	0.000 (13)	0.005 (15)	0.336 (15)
	17	J. Ma <i>et al.</i>	0.142 (17)	34.527 (17)	0.685 (17)	51 (15)	-0.066 (13)	0.013 (16)	0.000 (13)	0.000 (16)	0.049 (16)

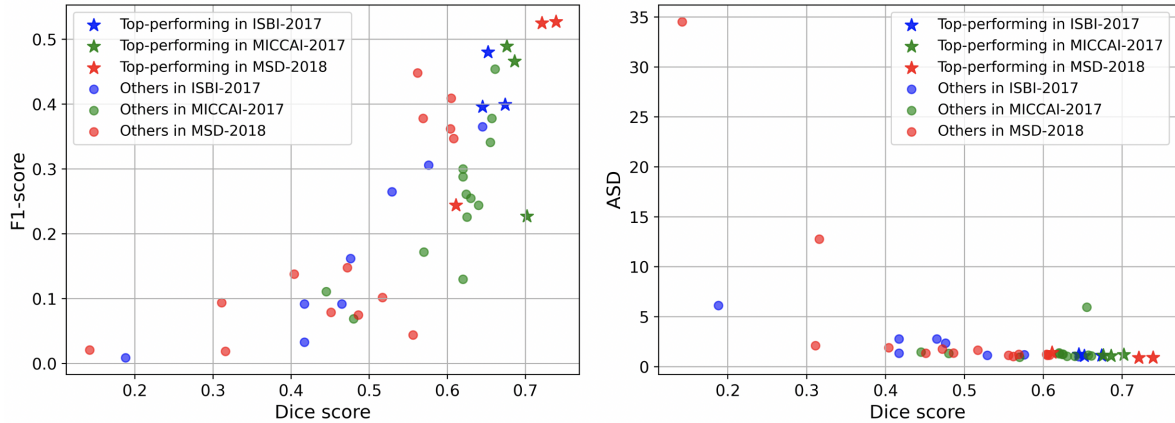


Figure 2: Scatter plots of methods’ performances considering: a) both segmentation and detection, b) both distance- and overlap-based metrics for three challenge events. We observe that not all the top-performing methods in three LiTS challenges achieved good scores on tumor detection. The behavior of distance- and overlap-based metrics is similar.

4.3.1. Inter-rater agreement

To better interpret the algorithmic variability and performance, we recruited another radiologist (Z. Z.) with >3 years of experience in oncologic imaging to re-annotate 15 3D CT scans, and two board-certified radiologists (J. K. and B. W.) to re-evaluate the original annotations. In Figure 3, R2 re-annotated 15 CT scans from scratch. R3 and R4 are board-certified radiologists who checked and corrected the annotations. Specifically, one board-certified radiologist (R3) reviewed and corrected existing annotations. R4 re-evaluated R3’s final annotations and corrected them. The inter-rater agreement was calculated by the Dice score per case between the pairs of two raters. We observed high inter-rater variability (median Dice of 70.2%) between the new annotation (R2) and the existing consensus annotation. We observed very high agreement (median Dice of 95.2%) between the board-certified radiologist and the existing annotations. Considering that the segmentation models were solely optimized on R1 and the best model achieved 82.5% on the leader-board (last access: 04.04.2022), we argue that there is still room for improvement.

4.3.2. Performance improvement

Top-performing teams over three events. First, we plotted the scores of Dice and ASD for three top-performing teams over the three events, as shown in Figure 4. We observed incremental improvement (e.g., the median scores) over the three events. We further performed Wilcoxon signed-rank tests on the best teams (ranked by mean Dice) between each pair of two events. We observed that MSD’18 shows significant improvement against ISBI’17 on both metrics (see Table 8). For MSD’18, the submitted algorithms architectures were the same for all sub-tasks. They were trained individually for sub-tasks (e.g., liver, kidney, pancreas), focusing on the generalizability of segmentation models. The main advance was the advent of 3D deep learning models after 2017. Tables 4 and 5 show that most of the approaches were 2D and 2.5D

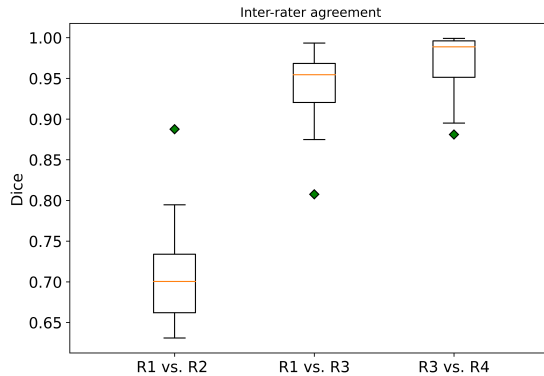


Figure 3: Inter-rater agreement between the existing annotation and new annotation sets. R1 represented the rater for the existing consensus annotation of the LiTS dataset. R2 re-annotated 15 CT scans from scratch. R3 and R4 are board-certified radiologists who checked and corrected the annotations. Specifically, one board-certified radiologist (R3) reviewed and corrected existing annotations. R4 re-evaluated R3’s final annotations and corrected them. The inter-rater agreement was calculated by the Dice score per case between the pairs of two raters.

Table 8: Results of Wilcoxon signed-rank tests between each pair of two events. MSD’18 significantly improved over ISBI’17 on both metrics.

p-value	MICCAI’17 vs. ISBI’17	MSD’18 vs. MICCAI’17	MSD’18 vs. ISBI’17
Dice	0.236	0.073	0.015
ASD	0.219	0.144	0.006

based. The winner of MSD - the nn-Unet approach was a 3D UNet based, self-configured and adaptive for specific tasks. We attributed the main improvement to the 3D architectures, which was in line with other challenges and benchmark results in medical image segmentation that occurred during this time.

CodaLab submissions in the last six years. First, we separated the submissions yearly and summarized them by individual violin plots shown in Figure 5. We observed a continuous improvement over the years, with the best results obtained in 2022. We excluded the submissions that achieved Dice scores $>10\%$ in the analysis. We further performed the Mann-Whitney U test on the distributions of mean Dice and ASD scores of all teams for each year. We observed that the scores achieved in 2022 are significantly better than in 2021, indicating that the LiTS challenge remains active and contributes to methodology development.

4.4. Technique trend and recent advances

We have witnessed that the released LiTS dataset contributes to novel methodology development in medical image segmentation in recent years. We reviewed sixteen papers that used the LiTS dataset for method development and evaluation from three sources: a) Journal of Medical Image Analysis (MIA), b) MICCAI conference proceeding, and c) IEEE Transaction on Medical Imaging (TMI), as shown in Table 10.

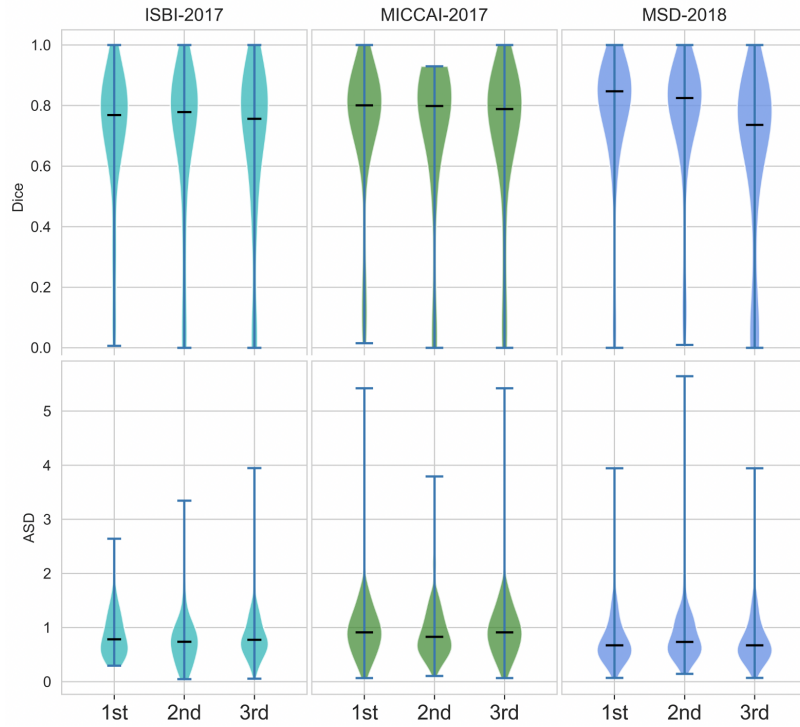


Figure 4: Dice and ASD scores of three top-performing teams over the three events.

Table 9: Results of Mann-Whitney U tests between the year of 2022 and the other years.

p-value	2022 vs. 2021	2022 vs. 2020	2022 vs. 2019	2022 vs. 2018	2022 vs. 2017
Dice	0.013	0.088	0.235	<0.001	0.024
ASD	0.002	0.158	0.129	<0.001	0.016

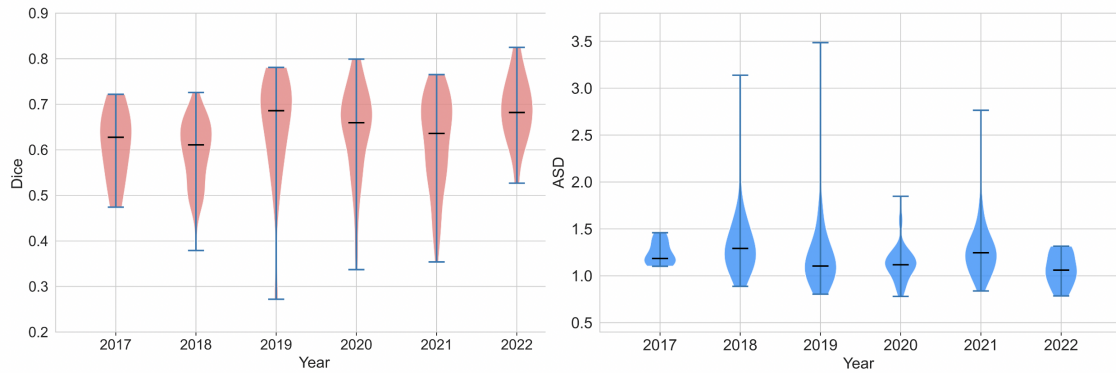


Figure 5: Distribution of mean Dice and ASD scores of all submissions in the CodaLab platform from the year 2017 to the year 2022.

A significant advance was on the 3D deep learning model besides the 2D approaches. [Zhou et al. \(2021b\)](#); [Haghighi et al. \(2021\)](#) proposed self-supervised pre-training frameworks to initialize 3D models for better

representation than training them from scratch. [Isensee et al. \(2020\)](#) proposed a self-configuring pipeline to facilitate the model training and the automated design of network architecture. [Wang et al. \(2019\)](#) added a 3D attention module for 3D segmentation models. These works improved the efficiency of 3D models and popularized the 3D models in many image segmentation tasks ([Ma, 2021](#)).

[Ma et al. \(2020\)](#) focused on the special trait of liver and liver tumor segmentation and proposed a novel active contour-based loss function to preserve the segmentation boundary. Similarly, [Tang et al. \(2020\)](#) proposed to enhance edge information and cross-feature fusion for liver and tumor segmentation. [Shirokikh et al. \(2020\)](#) considered the varying lesion sizes and proposed a loss reweighting strategy to deal with size imbalance in tumor segmentation. [Wang et al. \(2020\)](#) attempted to deal with the heterogeneous image resolution with a multi-branch decoder.

One emerging trend was leveraging available sparse labeled images to perform multi-organ segmentation. [Huang et al. \(2020\)](#) attempted to perform co-training of single-organ datasets (liver, kidney, and pancreas). [Fang & Yan \(2020\)](#) proposed a pyramid-input and pyramid-output network to condense multi-scale features to reduce the semantic gaps. Finally, [Yan et al. \(2020\)](#) developed a universal lesion detection algorithm to detect a variety of lesions in CT images in a multitask fashion and propose strategies to mine missing annotations from partially-labeled datasets.

4.4.1. Remaining challenges

Segmentation performance w.r.t. lesion size. Overall, the submitted methods performed very well for large liver tumors but struggled to segment smaller tumors (see Fig. 8). Many small tumors only have diameters of a few voxels; further, the image resolution is relatively high with 512×512 pixels in axial slices. Therefore, detecting such small structures is difficult due to the small number of potentially differing surrounding pixels, which can indicate a potential tumor border (see Fig. 8). It is exacerbated by the considerable noise and artifacts in medical imaging, which occur from size similarity; texture differences from the surrounding liver tissue and their arbitrary shapes are difficult to distinguish from an actual liver tumor. Overall, state-of-the-art methods performed well on volumes with large tumors and worse on volumes with small tumors. Worst results were achieved in exams where single small tumors ($<10\text{mm}^3$) occur. Best results were achieved when volumes showed less than six tumors with an overall tumor volume above 40mm^3 (see Fig. 8). In the appendix, we show the performance of all submitted methods of the three LiTS challenges, compared for every test volume, clustered by the number of tumor appearances and tumor sizes, see Figure A.10.

Segmentation performance w.r.t. image contrast. Another important influence of the methods' segmentation quality was the difference in tumor and liver HU values. Current state-of-the-art methods perform best for volumes showing higher contrast between liver and tumor. Especially in the case of focal lesions with a density 40-60 HU higher than that of the background liver (see Fig. 8). Worst results are achieved in

Table 10: Brief summary of sixteen published work using *LiTS* for the development of novel segmentation methods in medical imaging. While many of them focus on methodological contribution, they also advance the state-of-the-art in liver and liver tumor segmentation.

Source	Authors	Key Features
MIA	Zhou et al. (2021a)	multimodal registration, unsupervised segmentation, image-guided intervention
MIA	Wang et al. (2021)	conjugate fully convolutional network, pairwise segmentation, proxy supervision
MIA	Zhou et al. (2021b)	3D Deep learning, self-supervised learning, transfer learning
MICCAI	Shirokikh et al. (2020)	loss reweighting, lesion detection
MICCAI	Haghighi et al. (2020)	self-supervised learning, transfer learning, 3D model pre-training
MICCAI	Huang et al. (2020)	co-training of sparse datasets, multi-organ segmentation
MICCAI	Wang et al. (2019)	volumetric attention, 3D segmentation
MICCAI	Tang et al. (2020)	edge enhanced network, cross feature fusion
Nature Methods	Isensee et al. (2020)	self-configuring framework, extensive evaluation on 23 challenges
TMI	Cano-Espinosa et al. (2020)	biomarker regression and localization
TMI	Fang & Yan (2020)	multi-organ segmentation, multi-scale training, partially labeled data
TMI	Haghighi et al. (2021)	self-supervised learning, anatomical visual words
TMI	Zhang et al. (2020a)	interpretable learning, probability calibration
TMI	Ma et al. (2020)	geodesic active contours learning, boundary segmentation
TMI	Yan et al. (2020)	training on partially-labeled dataset, lesion detection, multi-dataset learning
TMI	Wang et al. (2020)	2.5D semantic segmentation, attention

cases where the contrast is below 20 HU (see Fig. 8), including tumors having a lower density than the liver. An average difference in HU values eases the network’s task of distinguishing liver and tumor since a simple threshold-derived rule could be applied as part of the decision process. Interestingly, an even more significant difference value did not result in an even better segmentation.

The performance of all submitted methods of three LiTS challenges was compared for every test volume, clustered by the HU level difference between liver and tumor and the HU level difference within tumor ROIs, shown in appendix Figure B.11.

5. Discussion

5.1. Limitations

The datasets were annotated by only one rater from each medical center. Thus it may introduce label bias, especially for small lesion segmentation, which is only ambiguous. However, further quality control of the annotations with consensus can reduce label noise and benefit supervised training and method evaluation. The initial rankings were conducted considering only the Dice score in which the large tissue will dominate. We observe that solely using Dice does not distinguish the top-performing teams but combining multiple metrics can do better. Unfortunately, imaging information (e.g., scanner type) and demographic information are unavailable when collecting the data from multiple centers. However, they are essential for in-depth analysis and further development of the challenge result (Maier-Hein et al., 2020; Wiesenfarth et al., 2021). The BIAS (Maier-Hein et al., 2020) report has proven to provide a good guideline for organizing a challenge

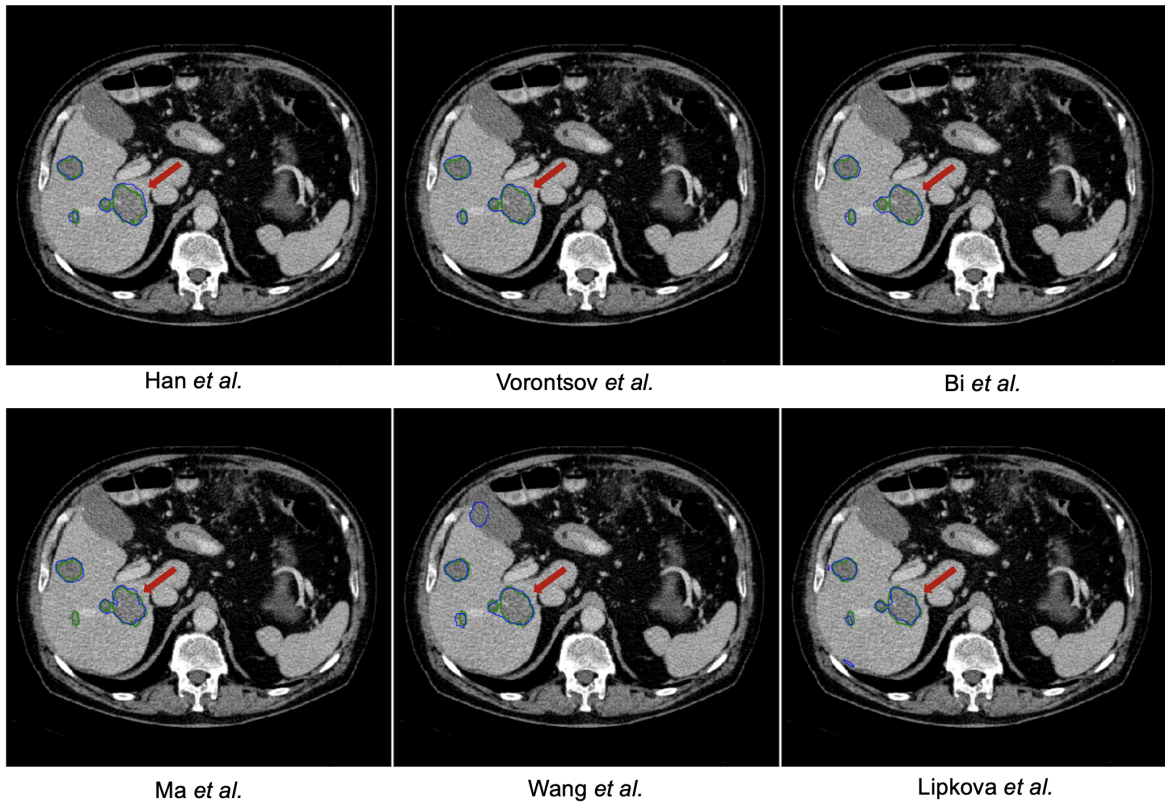


Figure 6: Tumor segmentation results of the ISBI-LiTS 2017 challenge. The reference annotation is marked with green contour, while the prediction is with blue contour. One could observe that the boundary of liver lesion is rather ambiguous.

and analyzing the outcome of the challenge. Tumor detection task is of clinical relevance, and the detection metric should be considered in future challenges.

To allow for quick evaluation of the submissions, we release the test data to the participant. Hence, we cannot prevent potential overfitting behavior by multiple iterative submissions or cheating behavior (e.g., manual correction of the segmentation). One option to improve this is using image containers (such as Docker ⁶ and Singularity ⁷) without releasing the test images. However, this would potentially limit the popularity of the challenge.

⁶<https://www.docker.com/>

⁷<https://sylabs.io/singularity/>

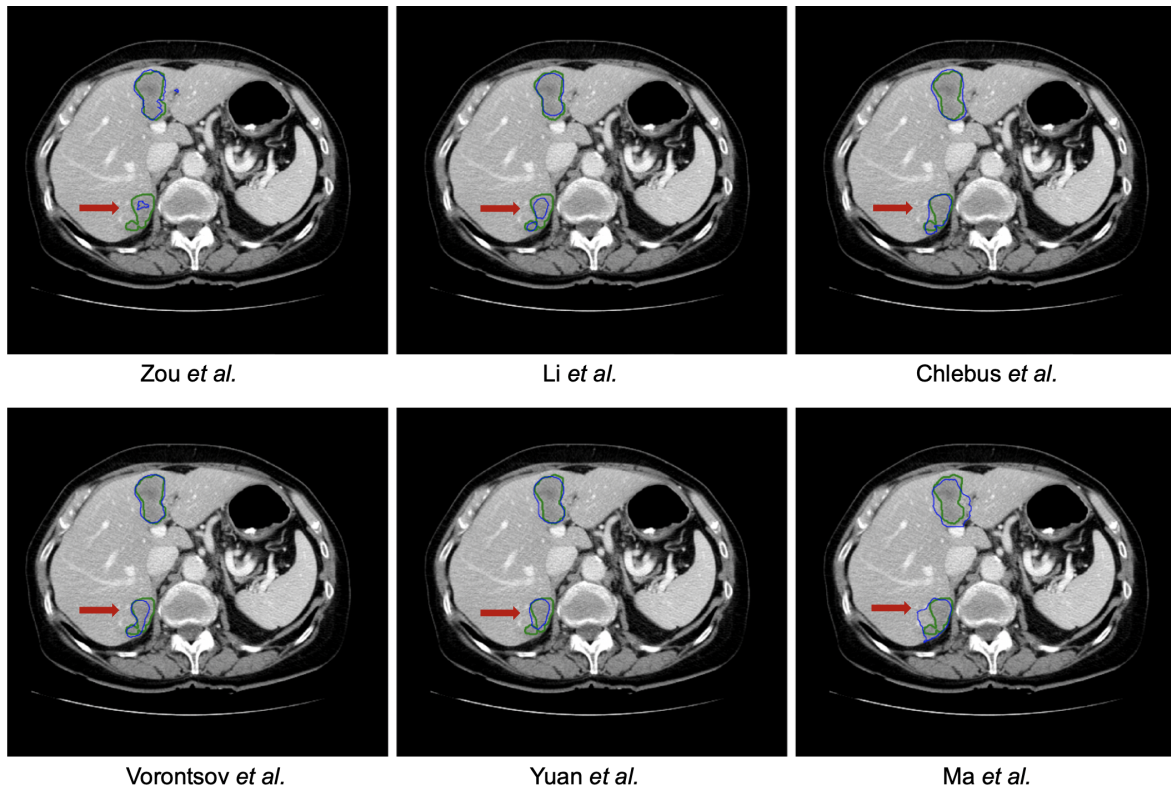
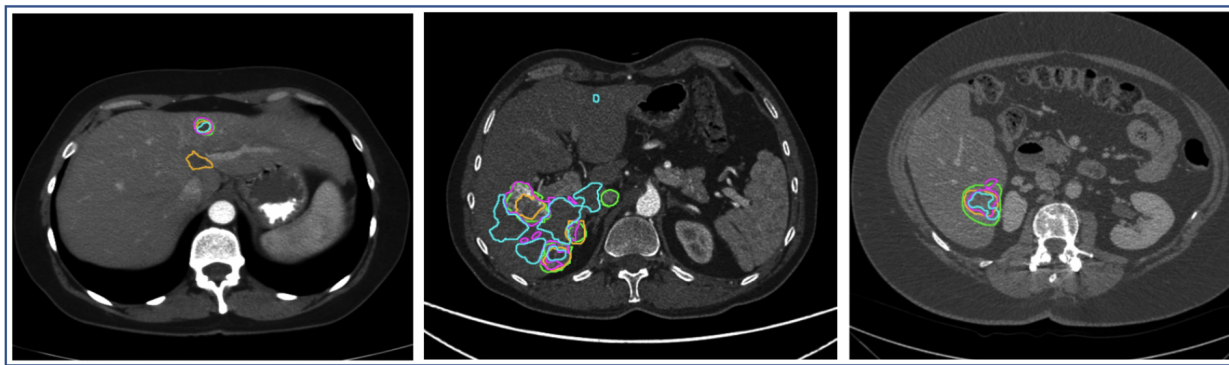
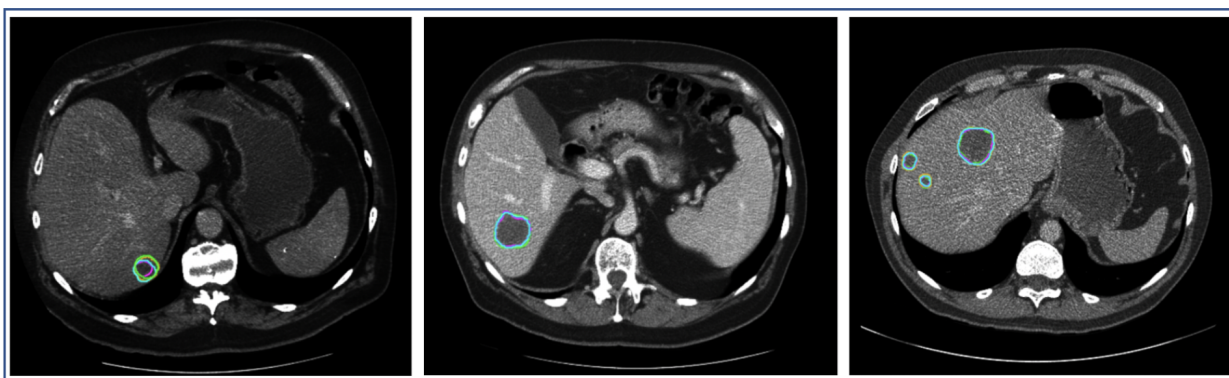


Figure 7: Tumor segmentation results of the MICCAI-LiTS 2017 challenge. The reference annotation is marked with green contour, while the prediction is with blue contour. One could observe that it is highly challenging to segment the liver lesion with poor contrast.

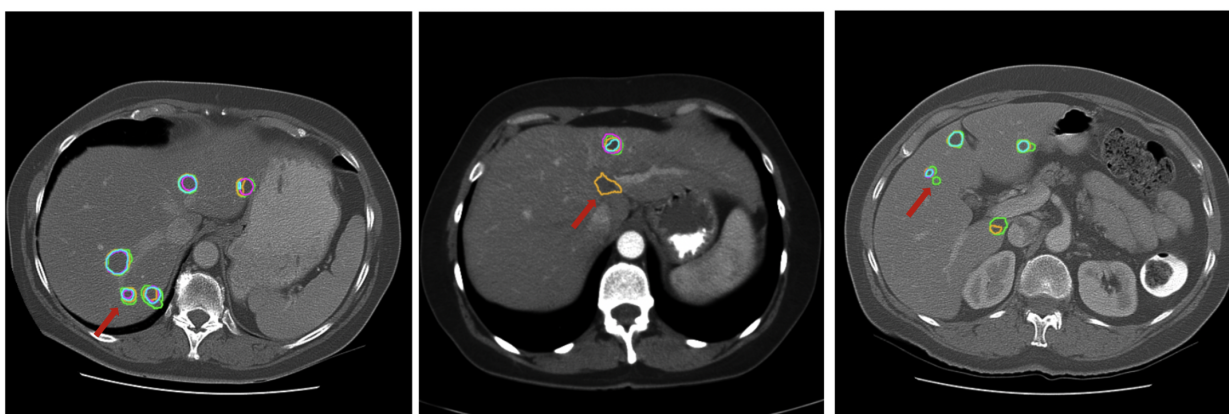


(a) Low HU value difference



(b) High HU value difference

Figure 8: Tumor segmentation results with selected cases of the tumor segmentation analysis regarding low (<20) and high (40-60) HU value difference. Compared are reference annotation (green), best-performing teams from ISBI 2017 (purple), MICCAI 2017 (orange), and MICCAI 2018 (blue). We can observe that a low HU value difference (<20) between tumor and liver tissue poses a challenge for tumor segmentation.



(a) Uncertainty

(b) False positive

(c) False negative

Figure 9: Samples of segmentation and detection results for small liver tumor. Compared are reference annotation (green), best-performing teams from ISBI 2017 (purple), MICCAI 2017 (orange), and MICCAI 2018 (blue).

5.2. Future work

Organizing LiTS has taught us lessons relevant for future medical segmentation benchmark challenges and their organizers. Given that many of the algorithms in this study offered good liver segmentation results compared to tumors, it seems valuable to evaluate liver tumor segmentation based on their different size, type, and occurrence per volume. Generating large labeled datasets is time-consuming and costly. It might be more efficiently performed by advanced semi-automated methods, thereby helping to bridge the gap to a fully automated solution.

Further, we recommend providing multiple reference annotations of liver tumors from multiple raters. This is because the segmentation of liver tumors presents high uncertainty due to the small structure and the ambiguous boundary (Schoppe et al., 2020). While most of the segmentation tasks in existing benchmarks are formulated to be one-to-one mapping problems, it does not fully solve the image segmentation problem where the data uncertainty naturally exists. Modeling the uncertainty in segmentation task is a trend⁸ (Mehta et al., 2020; Zhang et al., 2020b) and would allow the model generates not only one but various plausible outputs. Thus, it would enhance the applicability of automated methods in clinical practice. The released annotated dataset is not limited to benchmarking segmentation tasks but could also serve as data for recent shape modeling methods such as implicit neural functions (Yang et al., 2022; Kuang et al., 2022; Amiranashvili et al., 2021) Considering the size and, importantly, the demographic diversity of the patient populations from the seven institutions that contributed cases in the LiTS benchmark dataset, we think its value and contribution to medical image analysis will be greatly appreciated across numerous directions. One example use case is within the research direction of domain adaptation, where the LiTS dataset can be used to account for the apparent shift of the data distribution due to the domain change (e.g., acquisition setting) (Glocker et al., 2019; Castro et al., 2020). Another recent and intriguing use case is the research direction of federated learning, where the multi-institutional nature of the LiTS benchmark dataset could further contribute to federated learning simulations studies and benchmarks (Sheller et al., 2018, 2020; Rieke et al., 2020; Pati et al., 2021). It will target potential solutions to the LiTS-related tasks without sharing patient data across institutions. We consider federated learning of particular importance, as scientific maturity in this field could lead to a paradigm shift for multi-institutional collaborations. Furthermore, it is overcoming technical, legal, and cultural data sharing concerns since the patient involved in such collaboration will always be retained within their acquiring institutions.

Acknowledgement

Bjoern Menze is supported through the DFG funding (SFB 824, subproject B12) and a Helmut-Horten-Professorship for Biomedical Informatics by the Helmut-Horten-Foundation. Florian Kofler is Supported

⁸<https://qubiq.grand-challenge.org/Home/>

by Deutsche Forschungsgemeinschaft (DFG) through TUM International Graduate School of Science and Engineering (IGSSE), GSC 81. An Tang was supported by the Fonds de recherche du Québec en Santé and Fondation de l'association des radiologistes du Québec (FRQS-ARQ 34939 Clinical Research Scholarship – Junior 2 Salary Award). Hongwei Bran Li is supported by Forschungskredit (Grant NO. FK-21-125) from University of Zurich. We thank the CodaLab team, especially Eric Carmichael and Flavio Alexander for helping us with the setup.

References

- Abdel-massieh, N. H., Hadhoud, M. M., & Amin, K. M. (2010). Fully automatic liver tumor segmentation from abdominal ct scans. In *Computer Engineering and Systems (ICCES), 2010 International Conference on* (pp. 197–202). IEEE.
- Albain, K. S., Swann, R. S., Rusch, V. W., Turrisi, A. T., Shepherd, F. A., Smith, C., Chen, Y., Livingston, R. B., Feins, R. H., Gandara, D. R. et al. (2009). Radiotherapy plus chemotherapy with or without surgical resection for stage iii non-small-cell lung cancer: a phase iii randomised controlled trial. *The Lancet*, *374*, 379–386.
- Amiranashvili, T., Lüdke, D., Li, H., Zachow, S. et al. (2021). Learning shape reconstruction from sparse measurements with neural implicit functions. In *Medical Imaging with Deep Learning*.
- Antonelli, M., Reinke, A., Bakas, S., Farahani, K., Kopp-Schneider, A., Landman, B. A., Litjens, G., Menze, B., Ronneberger, O., Summers, R. M. et al. (2022). The medical segmentation decathlon. *Nature Communications*, *13*, 1–13.
- Bauknecht, H.-C., Romano, V. C., Rogalla, P., Klingebiel, R., Wolf, C., Bornemann, L., Hamm, B., & Hein, P. A. (2010). Intra- and interobserver variability of linear and volumetric measurements of brain metastases using contrast-enhanced magnetic resonance imaging. *Investigative radiology*, *45*, 49–56.
- Ben-Dan, I., & Shenhav, E. (2008). Liver tumor segmentation in ct images using probabilistic methods. In *MICCAI Workshop* (p. 43). volume 41.
- Blachier, M., Leleu, H., Peck-Radosavljevic, M., Valla, D.-C., & Roudot-Thoraval, F. (2013). The burden of liver disease in europe: a review of available epidemiological data. *Journal of hepatology*, *58*, 593–608.
- Bornemann, L., Dicken, V., Kuhnigk, J.-M., Wormanns, D., Shin, H.-O., Bauknecht, H.-C., Diehl, V., Fabel, M., Meier, S., Kress, O. et al. (2007). Oncotreat: a software assistant for cancer therapy monitoring. *International Journal of Computer Assisted Radiology and Surgery*, *1*, 231–242.
- Cano-Espinosa, C., González, G., Washko, G. R., Cazorla, M., & Estépar, R. S. J. (2020). Biomarker localization from deep learning regression networks. *IEEE transactions on medical imaging*, *39*, 2121–2132.
- Castro, D. C., Walker, I., & Glocker, B. (2020). Causality matters in medical imaging. *Nature Communications*, *11*, 1–10.
- Chlebus, G., Schenk, A., Moltz, J. H., van Ginneken, B., Hahn, H. K., & Meine, H. (2018). Automatic liver tumor segmentation in ct with fully convolutional neural networks and object-based postprocessing. *Scientific reports*, *8*, 1–7.
- Christ, P. F., Elshaer, M. E. A., Ettlinger, F., Tatavarty, S., Bickel, M., Bilic, P., Rempfler, M., Armbruster, M., Hofmann, F., D’Anastasi, M., Sommer, W. H., Ahmadi, S.-A., & Menze, B. H. (). Automatic liver and lesion segmentation in ct using cascaded fully convolutional neural networks and 3d conditional random fields. In *Medical Image Computing and Computer-Assisted Intervention – MICCAI 2016: 19th International Conference* (pp. 415–423).
- Ciecholewski, M., & Ogiela, M. R. (2007). Automatic segmentation of single and multiple neoplastic hepatic lesions in ct images. In *International Work-Conference on the Interplay Between Natural and Artificial Computation* (pp. 63–71). Springer.
- Cleary, K. (2017). Midas - original datasets. <http://insight-journal.org/midas/item/view/1346>. (Accessed on 01/12/2019).
- Conze, P.-H., Noblet, V., Rousseau, F., Heitz, F., De Blasi, V., Memeo, R., & Pessaux, P. (2017). Scale-adaptive supervoxel-based random forests for liver tumor segmentation in dynamic contrast-enhanced ct scans. *International journal of computer assisted radiology and surgery*, *12*, 223–233.
- Cootes, T. F., Taylor, C. J., Cooper, D. H., & Graham, J. (1995). Active shape models-their training and application. *Computer vision and image understanding*, *61*, 38–59.
- Dawant, B. M., Li, R., Lennon, B., & Li, S. (2007). Semi-automatic segmentation of the liver and its evaluation on the miccai 2007 grand challenge data set. *3D Segmentation in The Clinic: A Grand Challenge*, (pp. 215–221).
- Deng, X., & Du, G. (2008). 3d segmentation in the clinic: a grand challenge ii-liver tumor segmentation. In *MICCAI workshop*.
- Dou, Q., Chen, H., Jin, Y., Yu, L., Qin, J., & Heng, P.-A. (2016). 3d deeply supervised network for automatic liver segmentation from ct volumes. In *International Conference on Medical Image Computing and Computer-Assisted Intervention* (pp. 149–157). Springer.

- Eisenhauer, E., Therasse, P., Bogaerts, J., Schwartz, L., Sargent, D., Ford, R., Dancey, J., Arbuck, S., Gwyther, S., Mooney, M. et al. (2009). New response evaluation criteria in solid tumours: revised recist guideline (version 1.1). *European journal of cancer*, *45*, 228–247.
- Erickson, B., Kirk, S., Lee, Y., Bathe, O., Kearns, M., Gerdes, C., Rieger-Christ, K., & Lemmerman, J. (2016). Radiology data from the cancer genome atlas liver hepatocellular carcinoma [tcga-lihc] collection. *The Cancer Imaging Archive*, .
- Fang, X., & Yan, P. (2020). Multi-organ segmentation over partially labeled datasets with multi-scale feature abstraction. *IEEE Transactions on Medical Imaging*, *39*, 3619–3629.
- Glocker, B., Robinson, R., Castro, D. C., Dou, Q., & Konukoglu, E. (2019). Machine learning with multi-site imaging data: An empirical study on the impact of scanner effects. *arXiv preprint arXiv:1910.04597*, .
- Gobbi, P. G., Broglia, C., Di Giulio, G., Mantelli, M., Anselmo, P., Merli, F., Zinzani, P. L., Rossi, G., Callea, V., Iannitto, E. et al. (2004). The clinical value of tumor burden at diagnosis in hodgkin lymphoma. *Cancer: Interdisciplinary International Journal of the American Cancer Society*, *101*, 1824–1834.
- Haghighi, F., Taher, M. R. H., Zhou, Z., Gotway, M. B., & Liang, J. (2020). Learning semantics-enriched representation via self-discovery, self-classification, and self-restoration. In *International Conference on Medical Image Computing and Computer-Assisted Intervention* (pp. 137–147). Springer.
- Haghighi, F., Taher, M. R. H., Zhou, Z., Gotway, M. B., & Liang, J. (2021). Transferable visual words: Exploiting the semantics of anatomical patterns for self-supervised learning. *IEEE Transactions on Medical Imaging*, .
- Häme, Y. (2008). Liver tumor segmentation using implicit surface evolution. *The Midas Journal*, (pp. 1–10).
- Hann, L. E., Winston, C. B., Brown, K. T., & Akhurst, T. (2000). Diagnostic imaging approaches and relationship to hepatobiliary cancer staging and therapy. In *Seminars in surgical oncology* (pp. 94–115). Wiley Online Library volume 19.
- Heimann, T., Münzing, S., Meinzer, H.-P., & Wolf, I. (2007). A shape-guided deformable model with evolutionary algorithm initialization for 3d soft tissue segmentation. In *Information Processing in Medical Imaging* (pp. 1–12). Springer.
- Heimann, T., Van Ginneken, B., Styner, M., Arzhaeva, Y., Aurich, V., Bauer, C., Beck, A., Becker, C., Beichel, R., Bekes, G., Bello, F., Binnig, G., Bischof, H., Bornik, A., Cashman, P., Chi, Y., Córdova, A., Dawant, B., Fidrich, M., Furst, J., Furukawa, D., Grenacher, L., Hornegger, J., Kainmüller, D., Kitney, R., Kobatake, H., Lamecker, H., Lange, T., Lee, J., Lennon, B., Li, R., Li, S., Meinzer, H., Németh, G., Raicu, D., Rau, A., Van Rikxoort, E., Rousson, M., Ruskó, L., Saddi, K., Schmidt, G., Seghers, D., Shimizu, A., Slagmolen, P., Sorantin, E., Soza, G., Susomboon, R., Waite, J., Wimmer, A., & Wolf, I. (2009). Comparison and evaluation of methods for liver segmentation from ct datasets. *IEEE Transactions on Medical Imaging*, *28*, 1251–1265.
- Heimann, T., Wolf, I., & Meinzer, H.-P. (2006). Active shape models for a fully automated 3d segmentation of the liver—an evaluation on clinical data. *Medical Image Computing and Computer-Assisted Intervention–MICCAI 2006*, (pp. 41–48).
- Heussel, C. P., Meier, S., Wittelsberger, S., Götte, H., Mildenerger, P., & Kauczor, H.-U. (2007). Follow-up ct measurement of liver malignoma according to recist and who vs. volumetry. *RoFo: Fortschritte auf dem Gebiete der Rontgenstrahlen und der Nuklearmedizin*, *179*, 958–964.
- Hu, P., Wu, F., Peng, J., Liang, P., & Kong, D. (2016). Automatic 3d liver segmentation based on deep learning and globally optimized surface evolution. *Physics in Medicine & Biology*, *61*, 8676.
- Huang, R., Zheng, Y., Hu, Z., Zhang, S., & Li, H. (2020). Multi-organ segmentation via co-training weight-averaged models from few-organ datasets. In *International Conference on Medical Image Computing and Computer-Assisted Intervention* (pp. 146–155). Springer.
- Isensee, F., Jaeger, P. F., Kohl, S. A., Petersen, J., & Maier-Hein, K. H. (2020). nnu-net: a self-configuring method for deep learning-based biomedical image segmentation. *Nature Methods*, (pp. 1–9).
- Jagannath, S., Velasquez, W. S., Tucker, S. L., Fuller, L. M., McLaughlin, P. W., Manning, J. T., North, L. B., & Cabanillas, F. C. (1986). Tumor burden assessment and its implication for a prognostic model in advanced diffuse large-cell lymphoma.

- Journal of Clinical Oncology*, 4, 859–865.
- Jiménez Carretero, D., Fernández de Manuel, L., Pascau González Garzón, J., Tellado, J. M., Ramon, E., Desco Menéndez, M., Santos, A., & Ledesma Carbayo, M. J. (2011). Optimal multiresolution 3d level-set method for liver segmentation incorporating local curvature constraints, .
- Kainmüller, D., Lange, T., & Lamecker, H. (2007). Shape constrained automatic segmentation of the liver based on a heuristic intensity model. In *Proc. MICCAI Workshop 3D Segmentation in the Clinic: A Grand Challenge* (pp. 109–116).
- Kass, M., Witkin, A., & Terzopoulos, D. (1988). Snakes: Active contour models. *International journal of computer vision*, 1, 321–331.
- Kavur, A. E., Gezer, N. S., Barış, M., Aslan, S., Conze, P.-H., Groza, V., Pham, D. D., Chatterjee, S., Ernst, P., Özkan, S. et al. (2021). Chaos challenge-combined (ct-mr) healthy abdominal organ segmentation. *Medical Image Analysis*, 69, 101950.
- Kuang, K., Zhang, L., Li, J., Li, H., Chen, J., Du, B., & Yang, J. (2022). What makes for automatic reconstruction of pulmonary segments. *arXiv preprint arXiv:2207.03078*, .
- Kuhnigk, J.-M., Dicken, V., Bornemann, L., Bakai, A., Wormanns, D., Krass, S., & Peitgen, H.-O. (2006). Morphological segmentation and partial volume analysis for volumetry of solid pulmonary lesions in thoracic ct scans. *IEEE Transactions on Medical Imaging*, 25, 417–434.
- Lamecker, H., Lange, T., & Seebass, M. (2004). *Segmentation of the liver using a 3D statistical shape model*. Konrad-Zuse-Zentrum für Informationstechnik Berlin.
- Li, H., Jiang, G., Zhang, J., Wang, R., Wang, Z., Zheng, W.-S., & Menze, B. (2018a). Fully convolutional network ensembles for white matter hyperintensities segmentation in mr images. *NeuroImage*, 183, 650–665.
- Li, X., Chen, H., Qi, X., Dou, Q., Fu, C.-W., & Heng, P.-A. (2018b). H-denseunet: hybrid densely connected unet for liver and tumor segmentation from ct volumes. *IEEE transactions on medical imaging*, 37, 2663–2674.
- Li, Y., Hara, S., & Shimura, K. (2006). A machine learning approach for locating boundaries of liver tumors in ct images. In *null* (pp. 400–403). IEEE.
- Ling, H., Zhou, S. K., Zheng, Y., Georgescu, B., Suehling, M., & Comaniciu, D. (2008). Hierarchical, learning-based automatic liver segmentation. In *Computer Vision and Pattern Recognition, 2008. CVPR 2008. IEEE Conference on* (pp. 1–8). IEEE.
- Linguraru, M. G., Richbourg, W. J., Liu, J., Watt, J. M., Pamulapati, V., Wang, S., & Summers, R. M. (2012). Tumor burden analysis on computed tomography by automated liver and tumor segmentation. *Medical Imaging, IEEE Transactions on*, 31, 1965–1976.
- Litjens, G., Kooi, T., Bejnordi, B. E., Setio, A. A. A., Ciompi, F., Ghafoorian, M., van der Laak, J. A., van Ginneken, B., & Sánchez, C. I. (2017). A survey on deep learning in medical image analysis. *arXiv preprint arXiv:1702.05747*, .
- Lu, F., Wu, F., Hu, P., Peng, Z., & Kong, D. (2017). Automatic 3d liver location and segmentation via convolutional neural network and graph cut. *International journal of computer assisted radiology and surgery*, 12, 171–182.
- Ma, J. (2021). Cutting-edge 3d medical image segmentation methods in 2020: Are happy families all alike? *arXiv preprint arXiv:2101.00232*, .
- Ma, J., He, J., & Yang, X. (2020). Learning geodesic active contours for embedding object global information in segmentation cnns. *IEEE Transactions on Medical Imaging*, .
- Maier-Hein, L., Reinke, A., Kozubek, M., Martel, A. L., Arbel, T., Eisenmann, M., Hanbury, A., Jannin, P., Müller, H., Onogur, S. et al. (2020). Bias: Transparent reporting of biomedical image analysis challenges. *Medical image analysis*, 66, 101796.
- Massoptier, L., & Casciaro, S. (2007). Fully automatic liver segmentation through graph-cut technique. In *Engineering in Medicine and Biology Society, 2007. EMBS 2007. 29th Annual International Conference of the IEEE* (pp. 5243–5246). IEEE.

- Massoptier, L., & Casciaro, S. (2008). A new fully automatic and robust algorithm for fast segmentation of liver tissue and tumors from ct scans. *European radiology*, *18*, 1658.
- McKnight, P. E., & Najab, J. (2010). Mann-whitney u test. *The Corsini encyclopedia of psychology*, (pp. 1–1).
- Mehta, R., Filos, A., Gal, Y., & Arbel, T. (2020). Uncertainty evaluation metric for brain tumour segmentation. *arXiv preprint arXiv:2005.14262*, .
- Milletari, F., Navab, N., & Ahmadi, S.-A. (2016). V-net: Fully convolutional neural networks for volumetric medical image segmentation. In *2016 fourth international conference on 3D vision (3DV)* (pp. 565–571). IEEE.
- Moghbel, M., Mashohor, S., Mahmud, R., & Saripan, M. I. B. (2017). Review of liver segmentation and computer assisted detection/diagnosis methods in computed tomography. *Artif. Intell. Rev.*, (pp. 1–41).
- Moltz, J. H., Bornemann, L., Dicken, V., & Peitgen, H. (2008). Segmentation of liver metastases in ct scans by adaptive thresholding and morphological processing. In *MICCAI workshop* (p. 195). volume 41.
- Moltz, J. H., Bornemann, L., Kuhnigk, J.-M., Dicken, V., Peitgen, E., Meier, S., Bolte, H., Fabel, M., Bauknecht, H.-C., Hittinger, M. et al. (2009). Advanced segmentation techniques for lung nodules, liver metastases, and enlarged lymph nodes in ct scans. *IEEE Journal of selected topics in signal processing*, *3*, 122–134.
- Nordlinger, B., Guiguet, M., Vaillant, J.-C., Ballardur, P., Boudjema, K., Bachellier, P., & Jaeck, D. (1996). Surgical resection of colorectal carcinoma metastases to the liver: a prognostic scoring system to improve case selection, based on 1568 patients. *Cancer: Interdisciplinary International Journal of the American Cancer Society*, *77*, 1254–1262.
- Nugroho, H. A., Ihtatho, D., & Nugroho, H. (2008). Contrast enhancement for liver tumor identification. In *MICCAI workshop* (p. 201). volume 41.
- Osher, S., & Sethian, J. A. (1988). Fronts propagating with curvature-dependent speed: algorithms based on hamilton-jacobi formulations. *Journal of computational physics*, *79*, 12–49.
- Park, H., Bland, P. H., & Meyer, C. R. (2003). Construction of an abdominal probabilistic atlas and its application in segmentation. *IEEE Transactions on medical imaging*, *22*, 483–492.
- Pati, S., Baid, U., Zenk, M., Edwards, B., Sheller, M., Reina, G. A., Foley, P., Gruzdev, A., Martin, J., Albarqouni, S. et al. (2021). The federated tumor segmentation (fets) challenge. *arXiv preprint arXiv:2105.05874*, .
- Puesken, M., Buerke, B., Gerss, J., Frisch, B., Beyer, F., Weckesser, M., Seifarth, H., Heindel, W., & Wessling, J. (2010). Prediction of lymph node manifestations in malignant lymphoma: significant role of volumetric compared with established metric lymph node analysis in multislice computed tomography. *Journal of computer assisted tomography*, *34*, 564–569.
- Rey, D., & Neuhäuser, M. (2011). Wilcoxon-signed-rank test. In *International encyclopedia of statistical science* (pp. 1658–1659). Springer.
- Rieke, N., Hancox, J., Li, W., Milletari, F., Roth, H. R., Albarqouni, S., Bakas, S., Galtier, M. N., Landman, B. A., Maier-Hein, K. et al. (2020). The future of digital health with federated learning. *NPJ digital medicine*, *3*, 1–7.
- van Rikxoort, E., Arzhaeva, Y., & van Ginneken, B. (2007). Automatic segmentation of the liver in computed tomography scans with voxel classification and atlas matching. In *Proceedings of the MICCAI Workshop* (pp. 101–108). Citeseer.
- Ronneberger, O., Fischer, P., & Brox, T. (2015). U-net: Convolutional networks for biomedical image segmentation. In *MICCAI* (pp. 234–241). volume 9351.
- Saddi, K. A., Rousson, M., Chefd’hotel, C., & Cheriet, F. (2007). Global-to-local shape matching for liver segmentation in ct imaging. In *Proceedings of MICCAI workshop on 3D segmentation in the clinic: a grand challenge* (pp. 207–214).
- Schoppe, O., Pan, C., Coronel, J., Mai, H., Rong, Z., Todorov, M. I., Müskes, A., Navarro, F., Li, H., Ertürk, A. et al. (2020). Deep learning-enabled multi-organ segmentation in whole-body mouse scans. *Nature communications*, *11*, 1–14.
- Sheller, M. J., Edwards, B., Reina, G. A., Martin, J., Pati, S., Kotrotsou, A., Milchenko, M., Xu, W., Marcus, D., Colen, R. R. et al. (2020). Federated learning in medicine: facilitating multi-institutional collaborations without sharing patient data. *Scientific reports*, *10*, 1–12.

- Sheller, M. J., Reina, G. A., Edwards, B., Martin, J., & Bakas, S. (2018). Multi-institutional deep learning modeling without sharing patient data: A feasibility study on brain tumor segmentation. In *International MICCAI Brainlesion Workshop* (pp. 92–104). Springer.
- Shiina, S., Sato, K., Tateishi, R., Shimizu, M., Ohama, H., Hatanaka, T., Takawa, M., Nagamatsu, H., & Imai, Y. (2018). Percutaneous ablation for hepatocellular carcinoma: comparison of various ablation techniques and surgery. *Canadian Journal of Gastroenterology and Hepatology*, 2018.
- Shimizu, A., Narihira, T., Furukawa, D., Kobatake, H., Nawano, S., & Shinozaki, K. (2008). Ensemble segmentation using adaboost with application to liver lesion extraction from a ct volume. In *Proc. MICCAI Workshop on 3D Segmentation in the Clinic: A Grand Challenge II., NY, USA*.
- Shirokikh, B., Shevtsov, A., Kurmukov, A., Dalechina, A., Krivov, E., Kostjuchenko, V., Golanov, A., & Belyaev, M. (2020). Universal loss reweighting to balance lesion size inequality in 3d medical image segmentation. In *International Conference on Medical Image Computing and Computer-Assisted Intervention* (pp. 523–532). Springer.
- Slagmolen, P., Elen, A., Seghers, D., Loeckx, D., Maes, F., & Haustermans, K. (2007). Atlas based liver segmentation using nonrigid registration with a b-spline transformation model. In *Proceedings of MICCAI workshop on 3D segmentation in the clinic: a grand challenge* (pp. 197–206).
- Smeets, D., Stijnen, B., Loeckx, D., De Dobbelaer, B., & Suetens, P. (2008). Segmentation of liver metastases using a level set method with spiral-scanning technique and supervised fuzzy pixel classification. In *MICCAI workshop* (p. 43). volume 42.
- Soler, L., Delingette, H., Malandain, G., Montagnat, J., Ayache, N., Koehl, C., Dourthe, O., Malassagne, B., Smith, M., Mutter, D. et al. (2001). Fully automatic anatomical, pathological, and functional segmentation from ct scans for hepatic surgery. *Computer Aided Surgery*, 6, 131–142.
- Soler, L., Hostettler, A., Agnus, V., Charnoz, A., Fasquel, J., Moreau, J., Osswald, A., Bouhadjar, M., & Marescaux, J. (2010). 3d image reconstruction for comparison of algorithm database: a patient-specific anatomical and medical image database. ircad, strasbourg. *Tech. Rep.*, .
- Stewart, B. W., & Wild, C. P. (2014). *World cancer report 2014*. Technical Report WHO Press, World Health Organization.
- Tang, Y., Tang, Y., Zhu, Y., Xiao, J., & Summers, R. M. (2020). E⁺ net: An edge enhanced network for accurate liver and tumor segmentation on ct scans. In *International Conference on Medical Image Computing and Computer-Assisted Intervention* (pp. 512–522). Springer.
- Todorov, M., Paetzold, J. C., Schoppe, O., Tetteh, G., Shit, S., Efremov, V., Todorov-Völgyi, K., Düring, M., Dichgans, M., Piraud, M. et al. (2020). Machine learning analysis of whole mouse brain vasculature. *Nature methods*, 17, 442–449.
- Tomoshige, S., Oost, E., Shimizu, A., Watanabe, H., & Nawano, S. (2014). A conditional statistical shape model with integrated error estimation of the conditions; application to liver segmentation in non-contrast ct images. *Medical Image Analysis*, 18, 130–143.
- Jimenez-del Toro, O., Müller, H., Krenn, M., Gruenberg, K., Taha, A. A., Winterstein, M., Eggel, I., Foncubierta-Rodríguez, A., Goksel, O., Jakab, A. et al. (2016). Cloud-based evaluation of anatomical structure segmentation and landmark detection algorithms: Visceral anatomy benchmarks. *IEEE transactions on medical imaging*, 35, 2459–2475.
- Virdis, F., Reccia, I., Di Saverio, S., Tugnoli, G., Kwan, S., Kumar, J., Atzeni, J., & Podda, M. (2019). Clinical outcomes of primary arterial embolization in severe hepatic trauma: A systematic review. *Diagnostic and interventional imaging*, 100, 65–75.
- Vorontsov, E., Abi-Jaoudeh, N., & Kadoury, S. (2014). Metastatic liver tumor segmentation using texture-based omnidirectional deformable surface models. In *International MICCAI Workshop on Computational and Clinical Challenges in Abdominal Imaging* (pp. 74–83). Springer.
- Wang, R., Cao, S., Ma, K., Zheng, Y., & Meng, D. (2021). Pairwise learning for medical image segmentation. *Medical Image Analysis*, 67, 101876.

- Wang, S., Cao, S., Chai, Z., Wei, D., Ma, K., Wang, L., & Zheng, Y. (2020). Conquering data variations in resolution: A slice-aware multi-branch decoder network. *IEEE Transactions on Medical Imaging*, *39*, 4174–4185.
- Wang, X., Han, S., Chen, Y., Gao, D., & Vasconcelos, N. (2019). Volumetric attention for 3d medical image segmentation and detection. In *International Conference on Medical Image Computing and Computer-Assisted Intervention* (pp. 175–184). Springer.
- Wang, X., Yang, J., Ai, D., Zheng, Y., Tang, S., & Wang, Y. (2015). Adaptive mesh expansion model (amem) for liver segmentation from ct image. *PloS one*, *10*, e0118064.
- Wen, J., Zhang, X., Xu, Y., Li, Z., & Liu, L. (2009). Comparison of adaboost and logistic regression for detecting colorectal cancer patients with synchronous liver metastasis. In *Biomedical and Pharmaceutical Engineering, 2009. ICBPE'09. International Conference on* (pp. 1–6). IEEE.
- Wiesenfarth, M., Reinke, A., Landman, B. A., Eisenmann, M., Saiz, L. A., Cardoso, M. J., Maier-Hein, L., & Kopp-Schneider, A. (2021). Methods and open-source toolkit for analyzing and visualizing challenge results. *Scientific reports*, *11*, 1–15.
- Wu, W., Zhou, Z., Wu, S., & Zhang, Y. (2016). Automatic liver segmentation on volumetric ct images using supervoxel-based graph cuts. *Computational and mathematical methods in medicine*, *2016*.
- Xu, Z., Burke, R. P., Lee, C. P., Baucom, R. B., Poulouse, B. K., Abramson, R. G., & Landman, B. A. (2015). Efficient multi-atlas abdominal segmentation on clinically acquired ct with simple context learning. *Medical image analysis*, *24*, 18–27.
- Yan, K., Cai, J., Zheng, Y., Harrison, A. P., Jin, D., Tang, Y.-b., Tang, Y.-X., Huang, L., Xiao, J., & Lu, L. (2020). Learning from multiple datasets with heterogeneous and partial labels for universal lesion detection in ct. *IEEE Transactions on Medical Imaging*, .
- Yang, J., Wickramasinghe, U., Ni, B., & Fua, P. (2022). Implicitatlas: Learning deformable shape templates in medical imaging. In *Proceedings of the IEEE/CVF Conference on Computer Vision and Pattern Recognition* (pp. 15861–15871).
- Yushkevich, P. A., Piven, J., Hazlett, H. C., Smith, R. G., Ho, S., Gee, J. C., & Gerig, G. (2006). User-guided 3d active contour segmentation of anatomical structures: significantly improved efficiency and reliability. *Neuroimage*, *31*, 1116–1128.
- Zhang, F., Dvornek, N., Yang, J., Chapiro, J., & Duncan, J. (2020a). Layer embedding analysis in convolutional neural networks for improved probability calibration and classification. *IEEE transactions on medical imaging*, *39*, 3331–3342.
- Zhang, L., Tanno, R., Xu, M.-C., Jacob, J., Ciccarelli, O., Barkhof, F., & Alexander, D. C. (2020b). Disentangling human error from the ground truth in segmentation of medical images. *arXiv preprint arXiv:2007.15963*, .
- Zhang, L., & Yu, S. C.-H. (2021). Context-aware polyunet for liver and lesion segmentation from abdominal ct images. *arXiv preprint arXiv:2106.11330*, .
- Zhang, X., Tian, J., Deng, K., Wu, Y., & Li, X. (2010). Automatic liver segmentation using a statistical shape model with optimal surface detection. *IEEE Transactions on Biomedical Engineering*, *57*, 2622–2626.
- Zhou, B., Augenfeld, Z., Chapiro, J., Zhou, S. K., Liu, C., & Duncan, J. S. (2021a). Anatomy-guided multimodal registration by learning segmentation without ground truth: Application to intraprocedural cbct/mr liver segmentation and registration. *Medical image analysis*, *71*, 102041.
- Zhou, X., Kitagawa, T., Hara, T., Fujita, H., Zhang, X., Yokoyama, R., Kondo, H., Kanematsu, M., & Hoshi, H. (2006). Constructing a probabilistic model for automated liver region segmentation using non-contrast x-ray torso ct images. *Medical Image Computing and Computer-Assisted Intervention–MICCAI 2006*, (pp. 856–863).
- Zhou, Z., Sodha, V., Pang, J., Gotway, M. B., & Liang, J. (2021b). Models genesis. *Medical image analysis*, *67*, 101840.

CRedit Author Statement

Partick Christ: Conceptualization, Writing Original Draft, Data Curation, Visualization, Software, Validation, Investigation.

Bjoern Menze: Conceptualization, Writing - Review & Editing, Data Curation, Visualization, Supervision, Investigation.

Partick Bilic: Writing, Data Curation, Visualization, Investigation.

Hongwei Bran Li: Writing, Revision, Corresponding, Visualization, Investigation.

Eugene Vorontsov: Writing, Visualization, Software, Investigation.

Rickmer Braren, Georgios Kaissis, Avi Ben-Cohen, Adi Szeskin, Colin Jacobs, Gabriel Efrain Humpire Mamani, Gabriel Chartrand, Fabian Lohöfer, Julian Holch, Wieland Sommer, Felix Hofmann, Alexandre Hostettler, Naama Lev-Cohain, Michal Drozdal, Michal Marianne Amitai, Refael Vivanti, Jacob Sosna, Volker Heinemann, Christopher Pal, An Tang, Samuel Kadoury, Luc Soler, Bram van Ginneken, Hayit Greenspan: Conceptualization, Data Curation, Writing - Reviewing & Editing

Ivan Ezhov, Anjany Sekuboyina, Fernando Navarro, Florian Kofler, Johannes C. Paetzold, Suprosanna Shit, Xiaobin Hu, Jana Lipková, Markus Rempfler, Marie Piraud, Jan Kirschke, Benedikt Wiestler, Zhiheng Zhang, Christian Hülsemeyer, Marcel Beetz, Florian Ettliger, Michela Antonelli, Woong Bae, Míriam Belver, Lei Bi, Hao Chen, Grzegorz Chlebus, Erik B. Dam, Qi Dou, Chi-Wing Fu, Bogdan Georgescu, Xavier Giró-i-Nieto, Felix Gruen, Xu Han, Pheng-Ann Heng, Jürgen Hesser, Jan Hendrik Moltz, Christian Igel, Fabian Isensee, Paul Jäger, Fucang Jia, Krishna Chaitanya Kaluva, Mahendra Khened, Ildoo Kim, Jae-Hun Kim, Sungwoong Kim, Simon Kohl, Tomasz Konopczynski, Avinash Kori, Ganapathy Krishnamurthi, Fan Li, Hongchao Li, Junbo Li, Xiaomeng Li, John Lowengrub, Jun Ma, Klaus Maier-Hein, Kevis-Kokitsi Maninis, Hans Meine, Dorit Merhof, Akshay Pai, Mathias Perslev, Jens Petersen, Jordi Pont-Tuset, Jin Qi, Xiaojuan Qi, Oliver Rippel, Karsten Roth, Ignacio Sarasua, Andrea Schenk, Zengming Shen, Jordi Torres, Christian Wachinger, Chunliang Wang, Leon Weninger, Jianrong Wu, Daguang Xu, Xiaoping Yang, Simon Chun-Ho Yu, Yading Yuan, Miao Yue, Liping Zhang: Writing - Review & Editing.

Appendix A. Segmentation performance w.r.t tumor size and number of tumors.

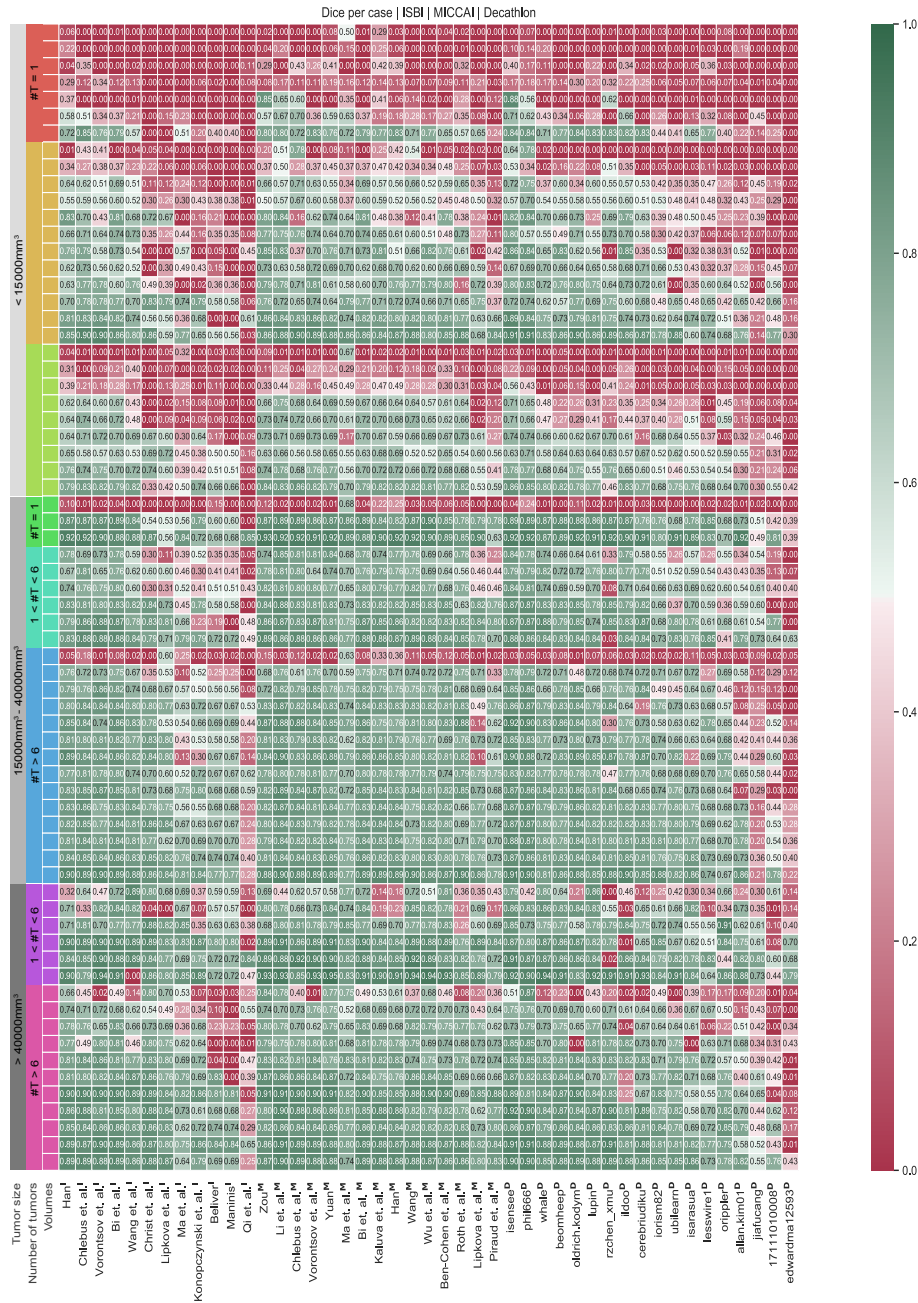


Figure A.10: Performance w.r.t tumor size and number of tumors. The test dataset is clustered by the number of tumors (#T) and size of the largest tumor per volume. Overall, participating methods perform well on volumes with large tumors and worse for volumes with small tumors. Worst results are achieved in chase where single small tumors (<15mm³) occur. Best results are achieved when volumes show less than 6 tumors with an overall tumor volume above 40mm³.

Appendix B. Segmentation performance w.r.t. HU value differences.

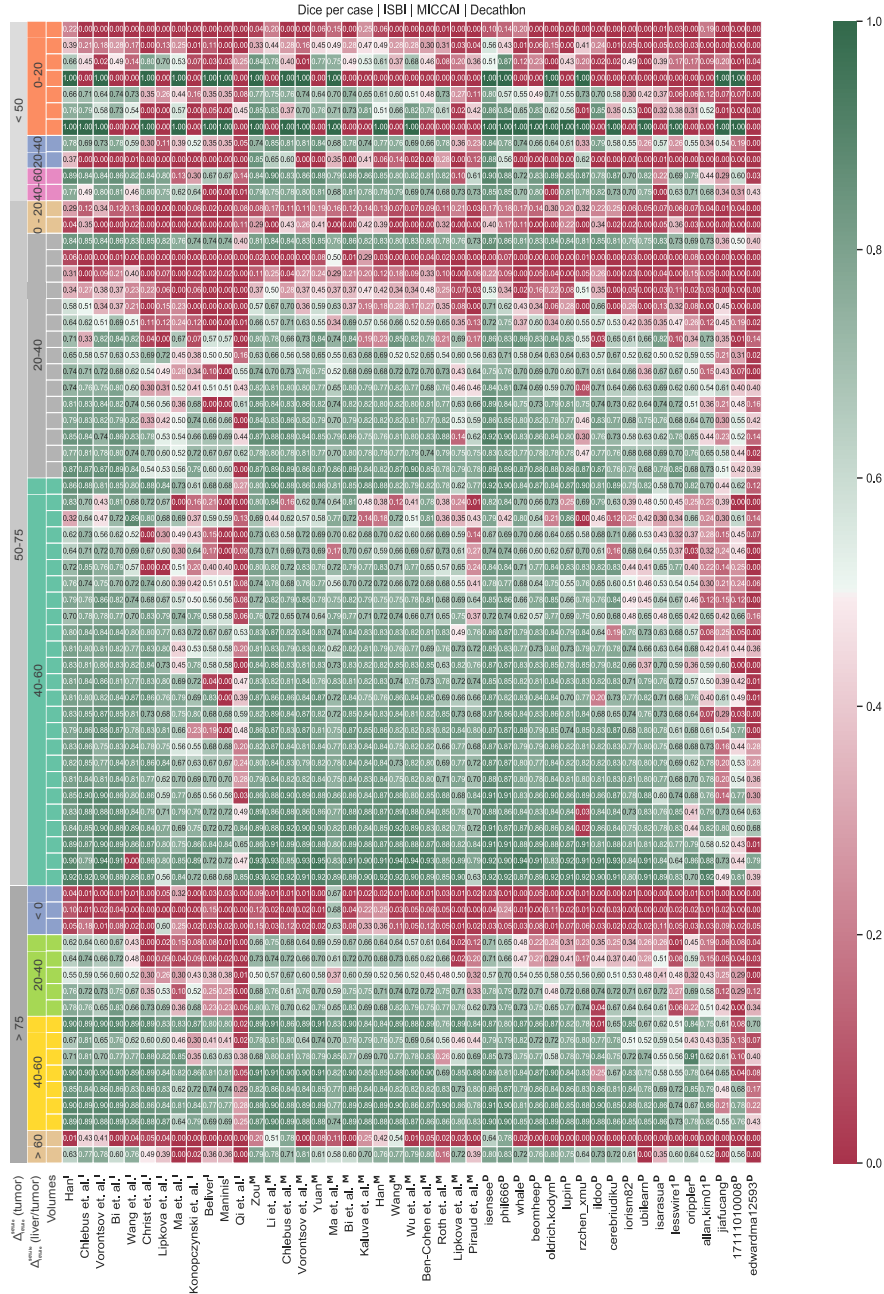


Figure B.11: Performance w.r.t HU value difference between tumor and non-tumor liver tissue. Two robust metrics are calculated to cluster the results on the test set. First, the HU value difference between liver and tumor is calculated using both regions' robust median absolute deviation per volume. Further, the clusters are split up by the tumor HU value difference calculated by the difference of the 90th percentile and 10th percentile. Participating methods perform best for volumes showing higher contrast between liver and tumor. Especially in the case of the liver, HU values are 40-60 points higher than the liver. Worst results are achieved in cases where the contrast is below 20 HU value, including tumors having a lower HU value than the liver.

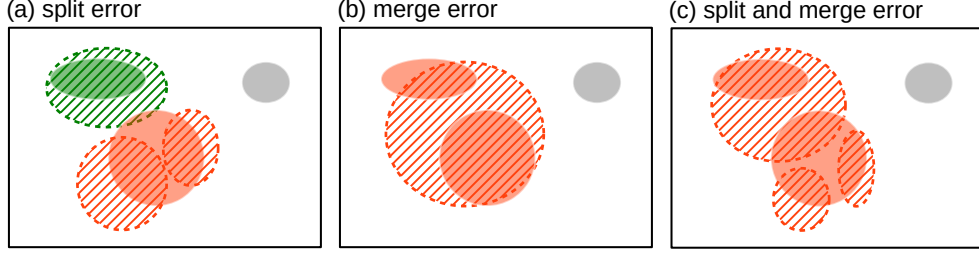


Figure C.12: Split and merge errors where a prediction splits a reference lesion into more than one connected component or merges multiple reference components into one, respectively. Reference connected components are shown with a solid color and predicted as regions with a dashed boundary and hatched interior. One-to-one correspondence is shown in green. One-to-two (a), two-to-one (b), and two-to-three (c) correspondence in orange. False negative in gray.

Appendix C. Correspondence algorithm

Components may not necessarily have a one-to-one correspondence between the two masks. For example, a single reference component can be predicted as multiple components (split error); similarly, multiple reference components can be covered by a single significant predicted component (merge error), as shown in Figure C.12.

Once connected components are found and enumerated in the reference and prediction masks, the correspondence algorithm determines the mapping between reference and prediction. Consider N_R connected components in the reference mask and N_P in the prediction mask. First, the many-to-many mapping is turned into a many-to-one mapping by merging all reference components \mathbf{r}_i ($i \in N_R$) that are connected by a single predicted component \mathbf{p}_j ($j \in N_P$), as shown in Figure C.13 (left). In the case where an \mathbf{r}_i overlaps multiple \mathbf{p}_j , the \mathbf{p}_j with the largest total intersected area is used. Thus, for every index $i \in N_R$, a corresponding $j_i \in N_P$ is determined as:

$$\forall i \in N_R, j_i = \begin{cases} \arg \max_j \mathbf{p}_j \cap \mathbf{r}_i, & \mathbf{p}_j \cap \mathbf{r}_i > 0 \\ \text{none}, & \text{else} \end{cases} \quad (\text{C.1})$$

and the \mathbf{r}_i are merged to ρ_j according to:

$$\rho_j = \bigcap_{i:j_i=j} \mathbf{r}_i, \quad (\text{C.2})$$

resulting in $N_\rho = |\{\rho_j\}|$ regions. Any \mathbf{r}_i without a corresponding \mathbf{p}_j is a false negative.

In the second step, the mapping is completed by associating each remaining \mathbf{p}_j with a single ρ_k ($k \in N_\rho$) with which it shares the largest total intersected area and merging all the \mathbf{p}_j that share the same ρ_k , as

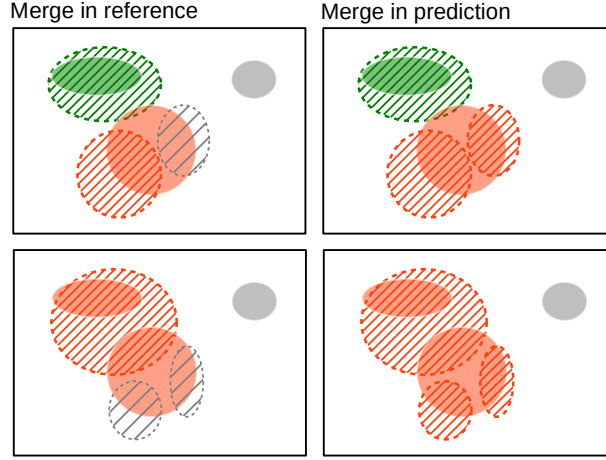


Figure C.13: Two examples (top and bottom) of the process to establish a correspondence between connected components in the reference and prediction masks. Reference: solid color; prediction: dashed boundary and hatched interior. Left: reference components merged if the same predicted component overlaps them. Right: predicted components are merged together if the same merged reference component overlaps them. Corresponding reference and predicted components share the same color (green, orange). An undetected reference component is shown in solid gray. During the merge of reference components (left), predicted components that do not have the most significant overlap with a reference component are left unmatched (gray, dashed, and hatched). Their mapping is completed during the merge of predicted components (right).

shown in Figure C.13 (right). Thus, for every index $j \in N_P$, a corresponding $k \in N_\rho$ is determined as:

$$\forall j \in N_P, k_j = \begin{cases} \arg \max_k \mathbf{P}_j \cap \rho_k, & \mathbf{P}_j \cap \rho_k > 0 \\ \text{none}, & \text{else} \end{cases} \quad (\text{C.3})$$

and the \mathbf{p}_j are merged to π_k according to:

$$\pi_k = \bigcap_{j:k_j=k} \mathbf{p}_j, \quad (\text{C.4})$$

resulting in $N_\pi = |\{\pi_k\}|$ regions. Any \mathbf{p}_j without a corresponding \mathbf{r}_i is a false positive.

The result is a map with a correspondence between sets of predicted components and sets of reference components. In order to maintain the immutability of the reference, any metrics evaluated on a set of merged reference components are attributed to each constituent reference component. For example, if two connected components in the reference mask are merged, and a Dice score of 0.7 is computed on the mask combining both components, then each component is considered to have a Dice score of 0.7. If the reference components were not merged, the errors computed for each of the two components would be exaggerated (e.g., 0.3 and 0.5 Dice).

Table D.11: Tumor burden ranking in MICCAI-LiTS 2017.

Ranking	Ref. Name	Institution	RMSE	Max Error
1	C. Li <i>et al.</i>	CUHK	0.015 (1)	0.062 (6)
2	J. Wu <i>et al.</i>	NJU	0.016 (2)	0.048 (2)
3	C. Wang <i>et al.</i>	KTH	0.016 (3)	0.058 (4)
4	Y. Yuan <i>et al.</i>	MSSM	0.017 (4)	0.049 (3)
5	J. Zou <i>et al.</i>	Lenovo	0.017 (5)	0.045 (1)
6	K. Kaluva <i>et al.</i>	Predible Health	0.020 (6)	0.090 (12)
7	X. Han <i>et al.</i>	Elektta Inc.	0.020 (7)	0.080 (10)
8	A. Ben-Cohen <i>et al.</i>	Uni Tel Aviv	0.020 (8)	0.070 (7)
9	G. Chlebus <i>et al.</i>	Fraunhofer	0.020 (9)	0.070 (8)
10	L. Zhang <i>et al.</i>	CUHK	0.022 (10)	0.074 (11)
11	E. Vorontsov <i>et al.</i>	MILA	0.023 (11)	0.112 (13)
12	J. Lipkova <i>et al.</i>	TUM	0.030 (12)	0.140 (14)
13	K. Roth <i>et al.</i>	Volume Graphics	0.030 (13)	0.180 (15)
14	M. Piraud <i>et al.</i>	TUM	0.037 (14)	0.143 (16)
15	Jin Qi	0.0420 (12)	0.0330 (2)	
16	L. Bi <i>et al.</i>	Uni Sydney	0.170 (15)	0.074 (9)
17	J. Ma <i>et al.</i>	NJUST	0.920 (16)	0.061 (5)

Appendix D. Automated tumor burden analysis in MICCAI-LiTS 2017

Motivation. The tumor burden, defined as the liver/tumor ratio, plays an essential role in surgical resection planning (Nordlinger *et al.*, 1996; Jagannath *et al.*, 1986). Instead of measuring diameters of target tumors, a fully volumetric segmentation of both the liver and its tumor and the subsequent tumor burden analysis offers valuable insights into the disease progression (Blachier *et al.*, 2013). Further, tumor burden is also essential in assessing the effectiveness of different treatments and can potentially replace the RECIST protocol (Gobbi *et al.*, 2004; Bornemann *et al.*, 2007; Heussel *et al.*, 2007; Kuhnigk *et al.*, 2006; Puesken *et al.*, 2010; Bauknecht *et al.*, 2010). A fully automated liver and tumor segmentation allows more straightforward computation of tumor burden and simplifies surgical liver resection planning.

Metrics. The tumor burden of the liver is a measure of the fraction of the liver afflicted by cancer. As a metric, we measure the root mean square error (RMSE) in tumor burden estimates from lesion predictions.

$$RMSE = \sqrt{\frac{1}{n} \sum_{i=1}^n (A_i - B_i)^2} \tag{D.1}$$

Results. The tumor burden was well predicted by many methods, with the best-performing method achieving the lowest RMSE of 0.015 and the lowest maximum error at 0.033 (Tab. D.11). There was a slight variation in RMSE values by the last. 15th method still obtains the fifth rank due to the high number of duplicates in the low range of values. In overall, methods achieving high Dice per case scores also obtained lower RMSE values. Only small correlation exists between RMSE and the maximum error ranking.